Optimal Image-Based Task-Sequence/Path Planning and Robust Hybrid Vision/Force Control of Industrial Robots

BAHAR AHMADI, **EHSAN ZAKERI**, AND **WEN-FANG XIE**, (Senior Member, IEEE)

Department of Mechanical, Industrial and Aerospace Engineering, Concordia University, Montreal, QC H3G 1M8, Canada

Corresponding author: Wen-Fang Xie (wfxie@encs.concordia.ca)

ABSTRACT In this paper, a novel image-based task-sequence/path planning scheme coupled with a robust vision/force control method is suggested for solving the multi-task operation problem of an eye-in-hand (EIH) industrial robot interacting with a workpiece. The proposed method suggests an optimal task sequence planning scheme to perform all the tasks and an optimal path planning method to generate a collision-free path between the tasks when the robot performs free-motion. To this end, a new method is presented which solves both problems simultaneously. A novel deadlock-free modified artificial potential field (MAPF) based on rotational potential force is developed for generating the collision-free path between tasks in the three-dimensional (3D) environment. The parameters of the MAPF and the sequence of the tasks are found by an optimizer simultaneously. This problem can be considered as a MAPF-constrained-generalized-traveling-salesman-problem (MAPF-CGTSP), which is a mix-integer optimization problem. The mix-integer version of multi-tracker optimization algorithm (MTOA) is developed to solve the problem. However, since image-based visual servoing (IBVS) is used for motion control, the planning is conducted in the image space. Integrated with the proposed planning method, a novel chattering-free filtered quasi sliding mode controller (FQSMC) is specially designed for robust vision/force control of the robot. FQSMC exploits a novel variable-gain orthogonal-sliding-manifold (VGOSM) which enables the robot to switch between free-motion mode and interaction mode. FQSMC overcomes large uncertainties and filters out the existing noises by exploiting an intrinsic filter within its control law. Experimental results show the superiority of the proposed approach to other state-of-the-art methods.

INDEX TERMS Optimal task-sequence/path planning, advanced artificial potential field, constrained generalized traveling salesman problem, robust hybrid vision/force control, filtered quasi-SMC.

I. INTRODUCTION

In many industrial robotic operations such as spot welding, milling, drilling, and electrical circuit soldering, the robot may need to interact with the workpiece several times on different paths or points, each of which can be considered as a task [1], [2]. To carry out such a multi-task operation, one solution is to consider each task as an individual operation. Then, the operator will program the robot to perform each task one-by-one, i.e., manual task planning. Although widely used, this method is time-consuming, and the operator's mistakes may result in a collision and damaging the workpiece. Therefore, planning an optimal sequence of the tasks and generating a collision-free path for performing free

motion between the tasks are crucial for industrial manufacturing to gain high productive, low cost, efficient, and safe operations [3].

The task sequence planning aims at determining the order of performing the tasks in a way that the overall operation time duration is minimized. Usually, the task sequence problem is defined as a traveling salesman problem (TSP) whose solution is the optimal sequence of the tasks. Depending on the tasks' types and constraints, different types of TSP problems, such as standard TSP [4], generalized TSP [5] and clustered TSP can be defined [1]. In [4], the task sequence problem of a fruit picking operation is addressed. To this end, the problem is directly formulated and solved as a standard TSP. In [5], robotic multi-hole drilling operation is addressed, where the robot task sequence problem is considered as a modified generalized TSP. In [1], a clustering-based TSP

algorithm is used to solve the task sequence problem of a robot manipulator for a large number of target points and greater spatial constraints in a cluttered environment. In these studies, the operational areas are assumed to be free of obstacles. In real operations, however, several obstacles may exist in the robot workspace. Therefore, the lack of designing a suitable path planning method between the tasks may result in collision or generation of non-optimal paths.

Path planning involves the strategy of generating the shortest path between the initial and destination positions while avoiding the obstacles under several constraints. Among different methods of path planning, artificial potential field (APF) method is one of the most well-known and feasible methods for generating a collision-free path. The basic concept of the APF method requires filling the activity area with the artificial potential field in which the agent is attracted to its target position, and is repulsed away from the obstacles and other agents [7]–[9]. In [7], a non-collision trajectory planning strategy based on APF is developed for path optimization of serial robots. In [8], a path planning method is proposed with an APF method for redundant robots. In [9], a new strategy is developed for assessing the collision risk and avoiding it using an APF and the fuzzy inference system. Although conventional APF is very effective for obstacle avoidance, it suffers from major drawbacks, the most important of which is trapping in local minima. This phenomenon is the result of aligning the repulsive and attractive force but in the opposite direction. Several approaches have been presented to address this problem. In [48], a new technique is employed to add repulsive force normal to the direction of attractive force which provides more flexibility for the APF method and results in the escaping from a local minimum. Another solution is to use metaheuristic optimization algorithms to set the parameters of the APF, to find a short path that reaches the target. In [47], a repulsive potential field is proposed by considering the relative distance between the robot and the target. Then it is optimized by using particle swarm optimization (PSO) to find the APF parameters in a way that an optimal path between the target and the departure point is generated. In [45] a dynamic membrane method combined with the pseudo-bacterial genetic algorithm for adjusting the parameters of APF is introduced to enhance the optimization procedure. In [46], a membrane evolutionary artificial potential field approach was proposed to solve the mobile robot route planning problem, which combines membrane computing with a genetic algorithm and the artificial potential field method to find the parameters to generate a feasible and safe route. The results show the superiority of the proposed method to the others.

Although all these studies have shown successful results, they are only applicable to single task operations. However, in [6], an integrated path planning and task sequencing approach is presented for robotic remote laser welding (RLW) operation, which is a multi-task operation. A TSP with neighborhoods and durative visits (TSP-ND) is defined to find the optimal path and sequence of tasks. However, the proposed

method cannot be adopted when physical interaction with the workpiece is required.

In addition to the path/sequence planning problem, interaction with a workpiece by an industrial robot is a challenging task that entails simultaneous control of the position of the end-effector and interaction force [10]. To this end, hybrid position/force control approach has been used in industries [10]–[14]. However, it requires the exact knowledge of the end-effector and workpiece, such as their poses and models, which may not be available [14].

To handle this issue, hybrid vision/force control has been suggested, in which a vision system provides non-contact measurement of some features of the workpiece or the end-effector [13]–[16]. Note that many studies have attempted to improve the overall performance of the visual servoing for a free-motion task and address the existing disadvantages [17], [18], while the research on advanced methods in the context of hybrid vision/force control is rare [13]–[16]. In [13], a camera with an eye-to-hand (ETH) configuration is used to estimate the position of the end effector. In [15] and [16], an eye-in-hand (EIH) camera is used to perform an image-based visual servoing (IBVS) in combination with force control. First, the system is decoupled into force and vision systems. Then two individual controllers are designed for each one. Using an EIH camera eliminates the necessity of knowing the workpiece's model. However, designing two separate controllers can be complex and time-consuming. Besides, the effect of uncertainties is not considered, and the overall controller's stability is not proved. To cope with this problem, employing sliding mode control method, would be an option to overcome large uncertainties and provide high tracking accuracy [20], [21], [37]. However, the conventional SMC suffers from chattering which emanates from a switching term within its control low. To handle this problem, several methods have been suggested such as higher-order and Quasi SMCs [20], [21]. Another problem with SMC is its susceptibility to noisy feedback. Usually, simple low-pass filters or Kalman filters can be used to tackle this problem. However, the performance of the control process may be degraded since these filters are not usually robust to uncertainties and also are not considered in the stability proof of the controller. Employing SMC for vision control systems using traditional image features is not feasible since their interaction matrix might be noninvertible [19]. This is the reason for the rareness of employing SMC in image-based visual servoing research studies.

Note that for hybrid vision/force manipulation with multiple tasks, the task-sequence/path planning must be carried out in the image feature space. Lots of research has been devoted to path planning in image space for pure visual servoing with different objectives [22], [23]. In [22], a path planning method is coupled with IBVS that suggests a modification of the projective interpolation algorithm that ensures the visibility of the target, while the camera calibration is not required. In [23], an image-based trajectory planning algorithm is proposed to avoid the problems caused by the camera's field of

view of IBVS methods by parametrizing the camera velocity screw utilizing time-based profiles. However, integrating task sequence/path planning with the vision/force control is a challenging task and to the best of our knowledge, such a strategy has not been suggested before. The reason is that the planning must be done in Cartesian space to gain an optimal path and avoid the collision, while in IBVS, the image feature feedback is employed, and the position of the end-effector cannot be measured directly in real-time. The fulfillment of the task demands a feasible method to map any arbitrary desired trajectory from Cartesian space to image feature space. It is noted that some mapping methods have been proposed such as learning by demonstration and spline fitting [24], [25]. However, these techniques cannot be utilized to map the specified paths as it is required for task sequence/path planning. In [24] a spline method has been developed to transform the desired trajectory from Cartesian space to the desired trajectory in image space. However, in this method, a new desired image feature path is required to be extracted corresponding to every different desired pose in the Cartesian space. The same method is suggested in [25]. However, no fitting method is used and the smoothed signals in the feature space are utilized instead. In addition to the mapping method, a technique should be integrated with the overall control law for managing the switching between the interaction and free-motion tasks. By employing such an algorithm, the robot can touch the surface or detach from it at the beginning and end of each task.

In this paper, to address all the mentioned issues of multi-task operation performed by an EIH industrial robot, a novel approach is developed. The proposed approach comprises two main parts: an optimal path/task sequence planning scheme and a robust hybrid vision/force control method.

Building upon the literature, a novel approach named modified APF-constrained generalized TSP (MAPF-CGTSP) is developed to solve the task sequence planning for multi-task operations with the optimal path length and obstacle avoidance. MAPF-CGTSP can be divided into two parts: a) modified APF (MAPF); and b) constrained generalized TSP (CGSTP).

MAPF is the modification of APF in which a rotational repulsive force is added to the repulsive force in 3D space. This repulsive force can be defined by two rotational parameters for each obstacle in the environment. If the parameters of the MAPF are adjusted properly, a deadlock-free path will be achieved. CGTSP is a TSP problem that can model multi-tasks operations sequence for an industrial robot. Employing MAPF for path planning between each two selected tasks by CGTSP results in MAPF-CGTSP model. Note that the parameters of MAPF are continuous while the sequence of the CGTSP is integers and binaries. Therefore, to adjust the parameters of the MAPF and find the optimal solution of CGTSP a mix-integer optimization algorithm can be employed. To this end, the mix-integer version of multi-tracker optimization algorithms (MTOA) is developed and applied to the problem [49]. Note that MTOA is

a population-based optimizer that can find the optimal solution with higher precision and reliability compared to those of the other well-known methods such as genetic algorithm (GA) [50], particle swarm optimization algorithm (PSO) [51], and grey wolf optimizer (GWO) [52]. The objective function of the optimization problem is the summation of the length of the paths between every two tasks generated using the MAPF and CGTSP sequence. When this function is minimized, i.e., MAPF-CGTSP is solved, an optimal path between the optimal sequence of the tasks is generated. Note that since IBVS method is used for controlling the robot, the initial position of the end-effector (IP) is unknown in the Cartesian space while it is known in the image feature space. Therefore, the cost value cannot be calculated in the cartesian space directly. To address this issue, first, the MAPF-CGTSP is transformed from the Cartesian space into image feature space. To this end, using the real data and a multi-layer perceptron neural network (MLP-NN) [26], [38], a novel method is developed to obtain the image features corresponding to the desired path in the Cartesian space. Then, the equivalent cost value will be calculated using the trajectories in the image feature space.

As mentioned before in the literature, the industrial robot in this study uses an eye-in-hand IBVS. The conventional IBVS methods are not suitable for tracking a trajectory on the image plan or performing a multi-task operation which needs switching between the free-motion and interaction with the workpiece several times. Therefore, in this paper, a novel filtered Quasi SMC (FQSMC) is designed for hybrid vision/force control. FQSMC exploits a variable-gain orthogonal sliding manifold (VGOSM) comprising orthogonal terms of force and vision errors with variable gains. Thus, the convergence of sliding manifold towards zero leads to the convergences of both force and vision errors towards zero. The variable gains in VGOSM also contribute to increasing the convergence speed, smaller tracking error, and preventing unwanted oscillation. Additionally, a binary contact variable is defined and incorporated in the VGOSM whose value changes when the robot performs free motion or interacts with the surface. A method is also developed to manage to switch between the free-motion and hybrid vision/force operations. FQSMC has a continuous output which results in Quasi-motion and elimination of chattering. Besides, by analyzing the control law of FQSMC, an intrinsic low-pass filter appears, which leads to filtering out the measurement noises associated with the camera and force sensor. Since the intrinsic filter is part of the control law, it will be involved in the stability proof and performance analysis.

The main contributions of this paper are listed as follows:
- Developing a new scheme called MAPF-CGTSP for image-based task sequence/path planning for multi-task operation of industrial robots.
- Presenting a new approach to obtain the image features corresponding to the desired path in the Cartesian space using a multi-layer perceptron neural network.
- Developing mix-integer MTOA to solve the optimization problem of MAPF-CGTSP.

- Designing a robust FQSMC with a novel VGOSM that enables the robot to perform free motion and interaction with the workpiece in the presence of uncertainties and noisy signals.

The rest of this paper is organized as follows. The system modeling and problem statement are described in section 2. Section 3 develops an optimal task sequence/path planning. The proposed hybrid controller is introduced in Section 4. Section 5 gives and discusses the experimental results. Conclusion remarks are drawn and presented in Section 6.

II. PROBLEM STATEMENT AND SYSTEM MODELING
In this section, the problem of performing a multi-task operation using IBVS and force control and system modeling is presented. First, different types of tasks are defined. Next, the modeling of a vision system is explained in detail and last, the interaction force modeling exerted on the workpiece is investigated.

A. PROBLEM STATEMENT
Referring to FIGURE 1.a, a six-DOF serial industrial robot equipped with a force sensor and an eye-in-hand (EIH) camera is considered. The workpiece is fixed with respect to the robot's reference frame. Also, a rectangular feature object is marked on the workpiece's surface whose corners are considered as four feature points (FIGURE 1.b). The surface of the workpiece satisfies $f_S(X_s) = 0$ where $f_S : \mathbb{R}^3 \to \mathbb{R}$ is the constraint function depending on the workpiece geometry; $X_s = (x_s, y_s, z_s)$ is the coordinate of any point on the workpiece's surface.

An operation may consist of two types of tasks: tasks in which the end-effector should interact with the workpiece while a) tracks a path; b) position to a single point. For the former tasks, the coordinates of one of the path's endpoints can be considered as the departure point and the other endpoint as the destination point. The desired tracking speed and the desired interaction force are dependent on the position of the tool-tip on the path. For the latter task, the duration of the regulation on the point is determined. Also, the desired interaction force could be chosen as a function of time. These tasks are defined as follows:

$$\text{Task } i: \begin{cases} \text{Type}: \begin{cases} 1, & \text{for point} \\ 2, & \text{for path} \end{cases} \\ P_{wd}(\vartheta) = \begin{bmatrix} f_x(\vartheta) & f_y(\vartheta) & f_z(\vartheta) \end{bmatrix}^T \\ \begin{cases} T_t, & \text{for point} \\ v_d(\vartheta), & \text{for path} \end{cases} \\ \begin{cases} F_{zd}(t), & \text{for point} \\ F_{zd}(\vartheta), & \text{for path,} \end{cases} \end{cases}$$
$$i = 1, 2, \ldots, n_T, \quad \vartheta = \begin{bmatrix} 0 & 1 \end{bmatrix}. \quad (1)$$

where n_T is the number of tasks, ϑ is an auxiliary variable which can vary from zero to one; $P_{wd}(\vartheta)$ is the desired path on the planar workpiece which is generated from the departure point to the destination point when ϑ changes from zero

to one; T_t is the duration of the interaction with the workpiece for the type 1 tasks, and $v_d(\vartheta)$ is the desired velocity for tracking the type 2 tasks. F_{zd} is the desired interacting force signal, which is the function of time or ϑ for type 1 and type 2 tasks, respectively. Note that $(f_x(\vartheta), f_y(\vartheta), f_z(\vartheta))$, i.e. the coordinate of a point on the predefined path of the task for $\vartheta \in \begin{bmatrix} 0 & 1 \end{bmatrix}$, must satisfy the surface constraint since the task is defined on the surface of the workpiece, i.e., $f_S(f_x(\vartheta), f_y(\vartheta), f_z(\vartheta)) = 0$.

The main objective of this paper is to develop an image-based task sequence/path planning coupled with a hybrid vision/force control method for the industrial robot to complete the entire multi-task operations effectively.

B. MODELING OF THE VISION SYSTEM
The kinematic relationship between the image feature vector and the camera frame $\{F_c\}$ is derived as follows [17], [18], [35], [36]:

$$\dot{S} = \mathbf{L}_s V \quad (2)$$

where $S \in \mathbb{R}^{n_f}$ is the vector of image features, n_f is the number of image features, $V \in R^6$ is the relative kinematic screw between the camera and the object (workpiece), and $\mathbf{L}_s \in \mathbb{R}^{n_f \times 6}$ is the interaction matrix. Note that the image features that are chosen for visual servoing of a 6-DOF robotic arm should correspond to the end-effector's pose, i.e., should map the projection of the end-effector trajectory from Cartesian space onto the camera image plane. A good feature point is one that can be located unambiguously in different views of the scene, such as the corners of the feature object. The image features parameters are defined to be any real-valued quantity that can be calculated from one or more image features, such as the distance between two points in the image plane and the orientation of the line connecting those two points [41], [42], perceived edge length [43], the area of a projected surface, the relative areas of two projected surfaces, or the centroid and higher-order moments of a projected object [35], [43], [44].

To have a unique solution for traditional IBVS and also prevent the singularity issue, one preferable choice is to adopt an object with at least four feature points (or eight image features) [35], [36]. However, in traditional IBVS, the main objective is to minimize the norm of image feature errors instead of converging them towards zero. This issue arises since $\mathbf{L}_S$ may not be invertible. In this case, the system is locally stable, and global stability cannot be guaranteed [17], [18]. Hence, employing advanced IBVS control strategies is not possible since the global stability of the closed-loop system is not ensured. To cope with this problem, a set of modified image features S suggested in [23] (please refer to FIGURE 1.b) is adopted as follows:

$$S = \begin{bmatrix} \bar{x}_c & \bar{y}_c & \overline{D}_c & \bar{\theta}_{cx} & \bar{\theta}_{cy} & \bar{\theta}_{cz} \end{bmatrix}^T \quad (3)$$

where:

$$\bar{x}_c = \frac{\sum_{i=1}^{4} x_{ci}}{4}, \quad \bar{y}_c = \frac{\sum_{i=1}^{4} y_{ci}}{4}$$

$$\overline{D}_c = \sum\nolimits_{i=1}^{3} \sqrt{(x_{ci+1} - x_{ci})^2 + (y_{ci+1} - y_{ci})^2}$$
$$+ \sqrt{(x_{c1} - x_{c4})^2 + (y_{c1} - y_{c4})^2}$$
$$\overline{\theta}_{cx} = \frac{1}{2}\left(\text{atan}\left(\frac{x_{c2} - x_{c1}}{y_{c1} - y_{c2}}\right) - \text{atan}\left(\frac{x_{c3} - x_{c4}}{y_{c4} - y_{c3}}\right)\right)$$
$$\overline{\theta}_{cy} = \frac{1}{2}\left(\text{atan}\left(\frac{y_{c3} - y_{c2}}{x_{c3} - x_{c2}}\right) - \text{atan}\left(\frac{y_{c4} - y_{c1}}{x_{c4} - x_{c1}}\right)\right)$$
$$\overline{\theta}_{cz} = \frac{1}{2}\left(\text{atan}\left(\frac{y_{c1} - y_{c4}}{x_{c4} - x_{c1}}\right) + \text{atan}\left(\frac{y_{c2} - y_{c3}}{x_{c3} - x_{c2}}\right)\right) \quad (4)$$

The image interaction matrix $\mathbf{L}_S$ corresponding to the image features of (3) has full-rank and thus can be invertible. The entries of $\mathbf{L}_S$ are available in [23]. The camera velocity screw is mapped to the joint space using the following relation:

$$V = \mathbf{J}_q \dot{q} \quad (5)$$

where $\mathbf{J}_q \in R^{6\times6}$ and $\dot{q} \in \mathbb{R}^{6\times1}$ are the robot Jacobian and vector of joint velocities, respectively [40]. Substituting (5) into (2) yields $\dot{S} = \mathbf{L}_s \mathbf{J}_q \dot{q}$. In the real applications, the uncertainties exist in the interaction matrix and Jacobian, i.e., $\mathbf{L}_s \mathbf{J}_q = \hat{\mathbf{L}}_s \hat{\mathbf{J}}_q + \delta_s$. Accordingly, the following relation yields:

$$\dot{S} = \hat{\mathbf{L}}_s \hat{\mathbf{J}}_q \dot{q} + \overline{\delta}_s \quad (6)$$

where, $\overline{\delta}_s = \delta_s \dot{q}$ is the uncertain part of the visual model, and notation $\hat{\ }$ denotes the nominal part.

C. INTERACTION FORCE MODELING

To design a force controller, the model of interaction between the tool and the workpiece should be derived. To this end, the stiffness model is exploited [27]. Accordingly, the mathematical formulation of the interacting force when the tool tip is in contact with the workpiece's surface is modeled as:

$$F = K_f P_f \quad (7)$$

where $K_f \epsilon \mathbb{R}^{6\times6}$ is the nominal diagonal stiffness matrix, P_f is the displacement vector, and F is the vector of forces and torques exerted to the tool. Taking time derivative of (7) yields:

$$\dot{F} = K_f V \quad (8)$$

Substituting (5) into (8) yields $\dot{F} = K_f \mathbf{J}_q \dot{q}$. Considering uncertainties in the kinematic relations and stiffness coefficient, i.e., $K_f \mathbf{J}_q = \hat{K}_f \hat{\mathbf{J}}_q + \delta_F$, which leads to the following relation:

$$\dot{F} = \hat{K}_f \hat{\mathbf{J}}_q \dot{q} + \overline{\delta}_F \quad (9)$$

where, $\overline{\delta}_F = \delta_F \dot{q}$ is the uncertain part of the interaction force model, and notation $\hat{\ }$ denotes the nominal part.

III. IMAGE-BASED TASK SEQUENCE/PATH PLANNING

To accomplish the multi-task operation, the robot should start from its initial position, select a task, and move towards the position above the start point of the path associated with the first task by a free motion. When the robot has fully converged to this position, the robot will move towards the
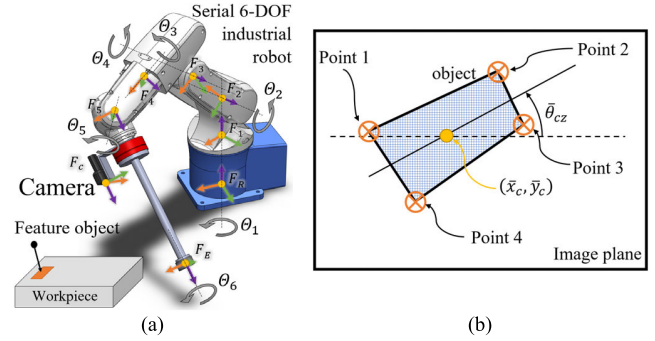

FIGURE 1. (a) Six-DOF industrial robot equipped with a force sensor and camera with EIH configuration. (b) Feature object in the image.

surface to come into contact with it. Then, the interaction begins, and the robot starts tracking the desired path and the force signal, simultaneously. When the path is tracked completely, the robot will detach from the surface and the first task is completed. Then the robot selects the next task, and the same procedure will be performed. This procedure continues till all tasks are completed. To make this procedure automatic, four main parts must be considered: a) an optimal task sequence/path planning method; b) a mechanism to contact with and/or detach from the workpiece's surface; c) a method to map the desired path from the Cartesian space to image space, and d) a proper vision/force control method for performing the tasks and free motions. The first three items are discussed in the following subsections and a novel hybrid control method will be presented in the next section.

A. OPTIMAL TASK SEQUENCING/PATH PLANNING

Planning the sequence of the tasks is of significant importance since between every two tasks there is a distance or path that the robot should pass to reach the next task with a free motion (pure IBVS). Optimal sequence planning would decrease the overall length of free motion distance and thereby reduce the operation time and energy consumption. At the same time, generating a feasible and safe path between the tasks and the avoidance of all obstacles in the environment is desired. Therefore, the combination of the task sequence and path planning for a multi-task operation result in decreasing the overall length of the path tracked by the robot for the whole operation. To this end, in this section, a hybrid optimal task sequence/path planning method is developed while avoiding the obstacles. First, the predefined tasks are described in the following subsections, and then, the task sequencing and path planning problems are presented in detail.

1) PREDEFINED TASKS

For type 1 task, the robot is controlled to the desired point. However, for type 2 task, the desired path should be transformed to the desired signals so that the robot can track it. Therefore, the following relation holds for the

desired path:

$$(v_d(\vartheta))^2 = \left(\left(\frac{\partial f_x(\vartheta)}{\partial \vartheta}\right)^2 + \left(\frac{\partial f_y(\vartheta)}{\partial \vartheta}\right)^2 \right.$$
$$\left. + \left(\frac{\partial f_z(\vartheta)}{\partial \vartheta}\right)^2\right)\left(\frac{d\vartheta}{dt}\right)^2 \qquad (10)$$

where v_d is the tracking velocity. According to (10), $\vartheta(t)$ is derived as follows:

$$\vartheta(t) = \int_0^t v_d(\vartheta)\left(\left(\frac{\partial f_x(\vartheta(t))}{\partial \vartheta(t)}\right)^2 + \left(\frac{\partial f_y(\vartheta(t))}{\partial \vartheta(t)}\right)^2 \right.$$
$$\left. + \left(\frac{\partial f_z(\vartheta(t))}{\partial \vartheta(t)}\right)^2\right)^{-\frac{1}{2}} dt \qquad (11)$$

By substituting $\vartheta(t)$, given in (11), into (1), the following desired signal is obtained:

$$P_{cd}(t) = \left[\begin{array}{cc}(P_{P_{cd}}(t))^{\mathrm{T}} & (P_{Ocd}(t))^{\mathrm{T}}\end{array}\right]^{\mathrm{T}},$$
$$P_{P_{cd}}(t) = \left[\begin{array}{ccc}f_x(\vartheta(t)) & f_y(\vartheta(t)) & f_z(\vartheta(t))\end{array}\right]^{\mathrm{T}},$$
$$P_{Ocd}(t) = \left[\begin{array}{ccc}\theta_{xd}(P_{P_{cd}}(t)) & \theta_{yd}(P_{P_{cd}}(t)) & \theta_{zd}(P_{P_{cd}}(t))\end{array}\right]^{\mathrm{T}}$$
$$(12)$$

where $(\theta_{xd}, \theta_{yd}, \theta_{zd})$ is the orientation of the end-effector obtained when the end-effector is normal to the workpiece surface on the interaction position, i.e., $rot(P_{Ocd}(t)) = \frac{Q_n(t)}{\|Q_n(t)\|}$ where $Q_n(t) = \left[\begin{array}{ccc}\frac{\partial f_S(x,y,z)}{\partial x} & \frac{\partial f_S(x,y,z)}{\partial y} & \frac{\partial f_S(x,y,z)}{\partial z}\end{array}\right]^{\mathrm{T}}$ at $P_{P_{cd}}(t)$ and $rot(.)$ is the rotation matrix of the end-effector.

2) TASK SEQUENCING PROBLEM

For each path, two points are considered above its end-points with a specific distance d_A called auxiliary end-point (AEP). These AEPs are the departure and destination points when the robot performs free motion for switching between the tasks. When a task completes, the tool-tip detaches from the workpiece and stays on the corresponding AEP. Then, another task is selected, and the robot moves towards the AEP corresponding to the next task to move downwards to the surface and start the interaction. This procedure continues till all tasks are done and the whole operation completes. As mentioned before, since the control process is carried out in feature space, the initial position of the end-effector is unknown in Cartesian space. Thus, to prevent the collision with the workpiece or obstacle at the beginning of the operation, a hypothetical box that encompasses the workpiece and the obstacles can be considered. The height of this box is higher than the workpiece's maximum height and the initial position of the end effector, i.e., IP, is assumed to be higher than the height of the hypothetical box. Then AEPs are extended to the top surface of the box (in the normal direction to the surface of the workpiece) and their intersections with that surface generate some new AEPs called NAEPs. Therefore, to prevent the collision, the robot tracks the line that connects the IP to the selected NAEP. Finally, the robot tracks the connecting
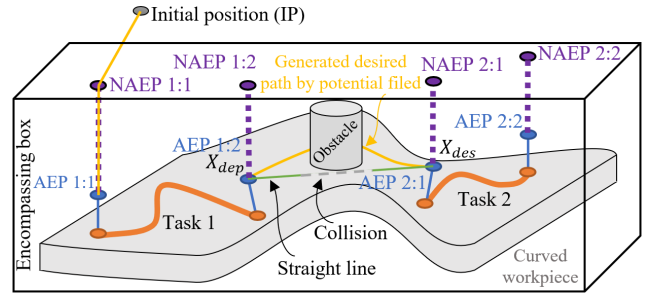

FIGURE 2. Task sequence planning in the workspace.

line from the NAEP to the corresponding AEP and continues the operation by selecting the AEPs of the remaining tasks (FIGURE 2).

The main objective of the task sequence planning, in this study, is to minimize the summation of path lengths between the AEPs of the tasks and the distance between the initial point of the tool-tip and the first AEP. Note that when a path is selected only one of the AEPs corresponding to its end-points can be selected which is the main property of generalized TSP (GTSP). Furthermore, if the selected task is tracking a path, one of its corresponding AEPs must be selected as the destination point and thus the other corresponding AEP is the departure point of the next sequence. However, if the selected task is a point, its corresponding AEP is considered as both the destination and departure points for the current and next sequences. Therefore, this is a constraint for the end-point selection corresponding to the task. Accordingly, the overall task sequence planning problem can be defined as a constrained GTSP (CGTSP) (FIGURE 3). The CGTSP is defined as follows,

$$\begin{aligned}
\mathrm{Min}: \quad & Cost_{\mathrm{CGTSP}} = \sum_{j=1}^{n_T}\sum_{l=1}^{2}\left(C_{j,l}d_{j,l}\right) \\
& + \sum_{i=1}^{n_T}\sum_{j=1}^{n_T}\sum_{k=1}^{2}\sum_{l=1}^{2}\left(C_{i,j,k,l}d_{i,j,k,l}\right), \\
\mathrm{Contraints}: \quad & \sum_{i=1}^{n_T}\sum_{k=1}^{2}\left(C_{i,k}\right) = 1; \\
& \sum_{i=1}^{n_T}\sum_{k=1}^{2}\sum_{l=1}^{2}\left(C_{i,j,k,l}\right) = 0; \\
& \sum_{i=1}^{n_T}\sum_{j=1}^{n_T}\sum_{k=1}^{2}\sum_{l=1}^{2}\left(C_{i,j,k,l}\right) \\
& = n_T - 1; \\
& \sum_{k=1}^{2}\sum_{l=1}^{2}\left(C_{i,j,k,l}\right) \le 1 \\
& \forall i \in \{1,\ldots,n_T\} \& j \in \{1,\ldots,n_T\} \qquad (13)
\end{aligned}$$

where $d_{i,j,k,l}$ is the length of the path between the kth AEP of the ith task and l^{th} AEP of the jth task which is calculated using MAPF explained in the next subsection; $d_{i j,l} = \|IP - AEP_{j,l}\|$ is the distance between the IP and the lth AEP of the jth task; $C_{i,j,k,l} \in \{0,1\}$ is the binary variable that indicates the connection from k^{th} AEP of the ith task to l^{th} AEP of the jth task, and $C_{i,j,l} \in \{0,1\}$ is the binary variable that indicates the connection from IP to l^{th} AEP of the jth task.
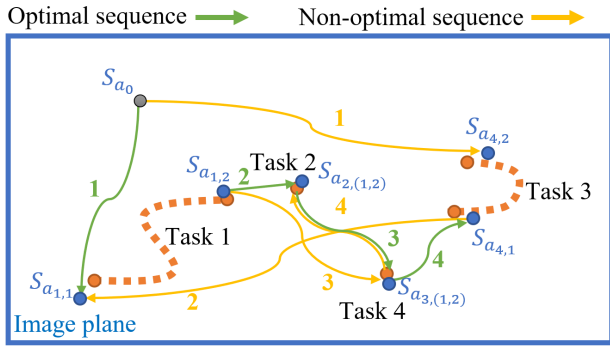
FIGURE 3. Task sequence planning in the image plane.

3) PATH PLANNING USING MAPF

In the manufacturing industry, the robots normally perform the operations on the workpieces with complex geometries. Thus, the ability to interact with these kinds of surfaces has been regarded as an important part of the industries [32]–[34].

For such workpieces, the free movement from one point to another cannot be performed on a straight line, due to the potential collision. To avoid the collision, the free motion must be done on a path that connects those two points (FIGURE 2).

For generating a collision-free path, APF method has been a prevailing method [30]. In APF, two kinds of potential fields are considered. a) attractive potential field towards the target destination AEP, i.e., $U_{att}(X)$; and b) repulsive potential fields from the surface of the object, i.e., $U_{rep}(X)$. Accordingly, the overall potential field $U(X)$ is obtained as:

$$U(X) = U_{att}(X) + U_{rep}(X) \qquad (14)$$

where $X \in \mathbb{R}^3$ is the coordinate of a point in the Cartesian space in the workpiece frame; $U_{att}(X)$ and $U_{rep}(X)$ are as follows:

$$U_{att}(X) = \frac{C_{p1}}{2} \|X - X_{des}\|^2,$$

$$U_{rep}(X) = \begin{cases} \dfrac{C_{p2}}{2} \left(\dfrac{1}{d_s} - \dfrac{1}{d_m} \right)^2, & d_s < d_m \\ 0, & d_s \geq d_m, \end{cases} \qquad (15)$$

where d_m is the thickness of the inadmissible layer on the surface and C_{Pi}, $i = 1, 2, 3$, are positive constants, X_{des} is the coordinates of the destination point and $d_s = \|X - X_n\|$ is the normal distance to the surface of the workpiece. X_n is the point on the surface, which has the minimum distance to X. Thus, X_n is the solution of $\begin{cases} f_S(x) = 0 \\ \dfrac{\partial f_d(x)}{\partial x} = 0 \end{cases}$ where $f_d(x) = \|X - x\|$.

According to *(14)* and *(15)*, the overall potential force is calculated as follows,

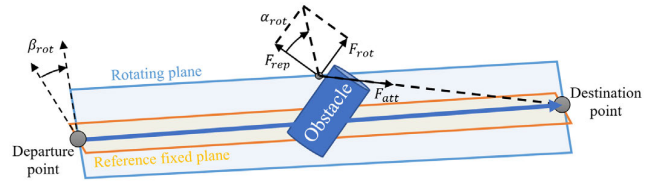$$F(X) = F_{att}(X) + F_{rep}(X) \qquad (16)$$

FIGURE 4. Rotational potential force.

where $F_{att}(X)$ and $F_{rep}(X)$ are the attractive and repulsive potential forces can be obtained as follows:

$$F_{att} = C_{p1}(X_{des} - X) \qquad (17)$$

$$F_{rep} = \begin{cases} C_{p2} \dfrac{1}{d_s^2} \left(\dfrac{1}{d_s} - \dfrac{1}{d_m} \right) \nabla_{d_s}, & d_s < d_m \\ 0, & d_s \geq d_m \end{cases} \qquad (18)$$

To generate the desired path from X_{dep} to X_{des}, the steepest decent method with a constant velocity v_m is adopted as follows:

$$X(t) = -\int_0^t \left(\frac{F(X)}{\|F(X)\|} v_m \right) dt + X_{dep}, \quad X(t_{des}) = X_{des} \qquad (19)$$

The main disadvantage of APF is its inability to escape from local minima. When repulsive force and attractive force has the same value but in the opposite direction, the equivalent force becomes zero and thus, it sticks in a local minimum point. One way to handle this issue is to use optimization algorithms to adjust the parameters, with the objective of reaching the destination point. However, due to the lack of flexibility, the solution for the optimization problem may not exist. To address this issue, in this paper, APF is modified by adding a rotational force in 3D space which leads to modified APF (MAPF). This rotational force contributes to escape from local minima by deviating the direction of the repulsive force and thus rounding the obstacle. Therefore, the overall potential force will not be zero in the points where the local minima occur and by adjusting the parameters properly, the problem of local minima can be solved. The direction of the rotational force is normal to the repulsive force and can be calculated as follows:

$$F_{rot}(X) = \frac{\tan(\alpha_{rot}) \cdot F_{rep}(X) \cdot \left(F_{rep}(X) \times N_{rot} \right)}{\left\| F_{rep}(X) \times N_{rot} \right\|} \qquad (20)$$

where N_{rot} is the vector normal to the plane that passes through the departure and destination points and is fixed with a specific angle β_{rot}. An example of the rotational force in 3D space is depicted in FIGURE 4. Therefore, the overall potential force can be rewritten as follows:

$$F(X) = F_{att}(X) + F_{rep}(X) + F_{rot}(X) \qquad (21)$$

4) CGTSP-MAPF

As mentioned before, to solve the CGTSP, the length of the paths between each task should be known. These paths, however, are generated using MAPF whose parameters should

be adjusted properly by an optimization algorithm. It is advantageous to merge both CGSTP and MAPF optimization problems as one optimization problem. Note that since the parameters of CGSTP and MAPF are binary and continuous, the resultant optimization problem would be a mix-integer one. To this end, a mix-integer version of MTOA is developed and employed to solve this problem which is discussed in the following subsections.

a: CGTSP-MAPF OPTIMIZATION PROBLEM

Since the control process is carried out in the image feature space, the generated path by MAPF must be transformed into this space. Besides, the initial pose of the end-effector in the Cartesian space is unknown. Thus, without the loss of generality, the paths between the AEPs in cartesian space are replaced with the corresponding trajectories in the image feature space whose length can be calculated as follows,

$$\overline{d_{ab}} = \int_0^{T_{\overline{ab}}} \left(S_{MAPF_{\overline{ab}}}^T \mathbf{W}_p S_{MAPF_{\overline{ab}}} \right) dt \qquad (22)$$

where $S_{MAPF_{\overline{ab}}} \in \mathbb{R}^6$ is the normal image feature vector corresponding to a point on the path between point a and b; and $\mathbf{W}_p \in \mathbb{R}^{6 \times 6}$ is the positive definite orthogonal matrix to be defined by the user. Note that S_{MAPF} is defined as follows:

$$S_{MAPF} = \left[\frac{\overline{x}_c}{\sqrt{\overline{D}_c}} \quad \frac{\overline{y}_c}{\sqrt{\overline{D}_c}} \quad \frac{\sqrt{\overline{D}_c}}{c_z} \quad \overline{\theta}_{cx} \quad \overline{\theta}_{cy} \quad \overline{\theta}_{cz} \right]^T \qquad (23)$$

where c_z is the coefficient of the depth in the image plane which is calculated based on the size of the image object. To map the generated path in the cartesian space to the image plane an MLP neural network is developed, which will be described in detail. It is worth mentioning that $\overline{d_{ab}}$ is a function of MAPF parameters, i.e., $\{C_{p1}, C_{p2_0}, \ldots, C_{p2_{n_o}}, \alpha_{rot_1}, \ldots, \alpha_{rot_{n_o}}, \beta_{rot_1}, \ldots, \beta_{rot_{n_o}}, d_{m_0}, \ldots, d_{m_{n_o}}\}$, which are adjusted by the optimization algorithm. Accordingly, based on (13), the overall CGSTP-MAPF optimization problem is derived as follows,

$$
\begin{aligned}
\text{Min:} \quad Cost_{\text{CGTS-MAPF}} &= \sum_{j=1}^{n_T} \sum_{l=1}^{2} \\
& \left(C_{j,l} \overline{di}_{j,l} \right) + \sum_{i=1}^{n_T} \sum_{j=1}^{n_T} \sum_{k=1}^{2} \\
& \sum_{l=1}^{2} \left(C_{i,j,k,l} \overline{d}_{i,j,k,l} \right),
\end{aligned}
$$

$$
\begin{aligned}
\text{Contraints:} \quad & \sum_{i=1}^{n_T} \sum_{k=1}^{2} \left(C_{i,k} \right) = 1; \\
& \sum_{i=1}^{n_T} \sum_{k=1}^{2} \sum_{l=1}^{2} \left(C_{i,j,k,l} \right) = 0; \\
& \sum_{i=1}^{n_T} \sum_{j=1}^{n_T} \sum_{k=1}^{2} \sum_{l=1}^{2} \\
& \left(C_{i,j,k,l} \right) = n_T - 1; \\
& \sum_{k=1}^{2} \sum_{l=1}^{2} \left(C_{i,j,k,l} \right) \leq 1 \\
& \forall i \in \{1, \ldots, n_T\} \, \& j \in \{1, \ldots, n_T\},
\end{aligned}
$$

Optimization Variables:

MAPF variables: $\{C_{p1}, C_{p2_0}, \ldots, C_{p2_{n_o}}, \alpha_{rot_1}, \ldots, \alpha_{rot_{n_o}}, \beta_{rot_1}, \ldots, \beta_{rot_{n_o}}, d_{m_0}, \ldots, d_{m_{n_o}}\} \in \mathbb{R}^+$

CGSTP variables: $Ci_{i,k} \in \{0, 1\}$ (24)

b: MIX-INTEGER MTOA

To solve the CGTSP-MAPF, the mix-integer version of MTOA is developed and employed. MTOA, which is a population-based optimization algorithm, was developed by Zakeri *et al.* in 2017 [53]. MTOA is composed of two types of trackers, global G_T and local L_T. During the search process, the global tracker, G_Ts, using stochastic motion and information from L_Ts, explore to find the global optimal point (GOP), *(25)*, [53]. The number of the local trackers is predetermined; each of them explores in a neighborhood of the corresponding G_T with radius R_S, *(26)*, to find the local optimal point, LP. The search radius around each G_T is determined by its rank, RK. The search process of this algorithm is described in detail in [53].

$$
\begin{aligned}
G_i &= \beta \left(GOP - G_{T_i} \right) + (1 - \beta) \left(LP_i - G_{T_i} \right), \\
& 0 \leq \beta \leq 1 \qquad (25) \\
Rs_i &= \begin{cases} Rf_i, & Rf_i \geq Rd_i \\ Rd_i, & Rf_i < Rd_i, \end{cases} \\
Rf &= \frac{RK_i - 1}{nop - 1} \cdot (RM - Rm) + Rm, \\
Rd_i &= \| G_{T_i} - GOP \| \qquad (26)
\end{aligned}
$$

where Rm and RM are the predefined minimum and maximum search radii, respectively. Note that to make MTOA applicable for integer optimization variables, the following relation has been used:

$$X_{int} = \frac{\left[X_{con} \cdot \left(1 + X_{int_{MAX}} - X_{int_{Min}} \right) \right]}{X_{con_{MAX}} - X_{con_{Min}}} + X_{int_{Min}} \qquad (27)$$

where [.] denotes the floor function, X_{con} and X_{int} are the continuous and integer variables for the optimization, respectively. $X_{con_{MAX}}$, $X_{con_{Min}}$, $X_{int_{MAX}}$, and $X_{int_{Min}}$ are the maximum and minimum of the continuous and integer variables, respectively.

B. MAPPING FROM CARTESIAN SPACE TO IMAGE PLANE

In IBVS, $S(t)$ is the set of image features corresponding to the pose of the camera (or end-effector) with respect to the workpiece frame $\{F_f\}$ at the time instant t, i.e., $P_c(t)$. However, defining $S_d(t)$, which is the set of desired image features corresponding to the desired pose $P_{cd}(t)$, is a challenging task. To this end, two main approaches have been suggested [25]: a) extracting analytical relationship between $P_{cd}(t)$ and $S_d(t)$; and b) experimental derivation of $S_d(t)$ when the camera pose is adjusted to $P_{cd}(t)$ manually, i.e., image trajectory planning based on robot programming by demonstration [25].

However, the first method may not be precise in the practice due to existing uncertainties in the camera's intrinsic and extrinsic parameters and the second method involves a cumbersome procedure which makes it inappropriate for tracking the desired paths. In this study, to handle these problems, the combination of these two methods is considered. First, the analytical relationship between $\hat{S}_d(t)$ and $P_{cd}(t)$ is derived. Then, $\hat{S}_d(t)$ passes through a three-layer multi-layer perceptron (MLP) neural network [26] whose output, $\overline{S}_d$, is the estimation of S_d. Then, the NN is trained to minimizing $e_{sd} = \overline{S}_d - S_d$.

Let $\hat{f}_{sd} : \mathbb{R}^6 \to \mathbb{R}^6$ be the analytical function that takes desired pose and returns estimated corresponding desired feature, i.e., $\hat{S}_d(t) = \hat{f}_{sd}(P_{cd}(t))$. Using NN, $\overline{S}_d$ is obtained as:

$$
\begin{aligned}
\overline{S}_d(t) &= \mathrm{NN_{sd}}\left(\hat{f}_{sd}(P_{cd}(t))\right) \\
&= \hat{f}_{sd}(P_{cd}(t)) + \mathbf{W_3}f_{sig}\left(\mathbf{W_2}f_{sig}\left(\mathbf{W_1}\hat{S}_d + B_1\right) + B_2\right) \\
&\quad + B_3
\end{aligned}
\tag{28}
$$

where, $f_{sig}(\star) = \frac{1}{1+e^{-\star}}$ is the sigmoid activation function. $\mathbf{W_1} \in \mathbb{R}^{n_1 \times 6}$, $\mathbf{W_2} \in \mathbb{R}^{n_2 \times n_1}$, and $\mathbf{W_3} \in \mathbb{R}^{6 \times n_2}$ are weight matrices and $B_1 \in \mathbb{R}^{n_1}$, $B_2 \in \mathbb{R}^{n_2}$, and $B_3 \in \mathbb{R}^6$ are the biases of the NN, all of which are tuned by training. n_1 and n_2 are the number of neurons in the first and second hidden layers. The topology of the adopted NN is illustrated in FIGURE 5.a.

To train the NN, a set of desired poses, P_{SD}, which are selected randomly with a uniform probability distribution in the workspace, is determined as follows:

$$
P_{SD} = \left\{ P_{R_1} \quad P_{R_2} \quad \cdots \quad P_{R_{n_d}} \right\}
\tag{29}
$$

where P_{R_1} to $P_{R_{n_d}}$ are the preselected desired poses, and n_d is the number of sampling data. Then, the sets of image features, S_{SD}, corresponding to P_{SD} are acquired as:

$$
S_{SD} = \left\{ S_{D_1} \quad S_{D_2} \quad \cdots \quad S_{D_{n_d}} \right\}
\tag{30}
$$

where S_{D_i} is the real image feature corresponding to P_{R_i} acquired in experiment. The pair of S_{SD} and P_{SD} can be used to train the NN using Levenberg-Marquardt (LM) method to minimize the following cost function [31]:

$$
\begin{aligned}
Cost = \sum_{i=1}^{n_d} \left(S_{D_i} - \mathrm{NN_{sd}}\left(P_{R_i}\right)\right)^{\mathrm{T}} \\
\times \mathbf{C_{NN}}\left(S_{D_i} - \mathrm{NN_{sd}}\left(P_{R_i}\right)\right)
\end{aligned}
\tag{31}
$$

where *Cost* is the cost function, and $\mathbf{C_{NN}} \in \mathbb{R}^{6 \times 6}$ is the diagonal positive definite matrix of cost value weight.

Besides the mapping network, an approach is needed to manage detachment from and contact with the workpiece's surface. The main desired path is defined on the workpiece's surface. Then, consider two other desired paths: one is rendered by moving the main desired path above the surface, called P_{d_F}, and the other beneath it, called P_{d_I}, with the margin shown in FIGURE 5.b The desired features corresponding to those paths are $\overline{S}_{d_F}$ and $\overline{S}_{d_I}$, respectively. Accordingly, if the robot needs to detach from the surface, i.e., free motion, $\overline{S}_{d_F}$ is selected and if the robot needs to interact with the
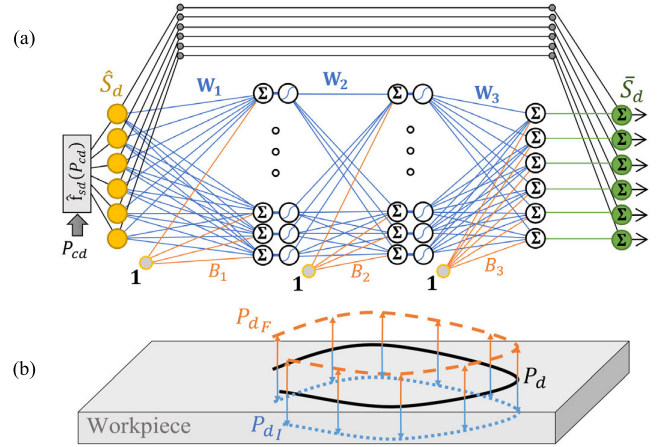

FIGURE 5. (a) The three-layer NN. (b) P_d, P_{D_F}, and P_{d_I}.

surface, $\overline{S}_{d_I}$ is chosen. Once the tool contacts with the surface, the binary switching variable $\psi \in \{0, 1\}$ is set to 1 and hybrid control is conducted, provided that $\overline{S}_{d_I}$ is selected as the desired path. Otherwise, $\psi = 0$ and free motion is carried out. This is done by incorporating ψ into the sliding variable which will be described in the next section. This procedure is presented in **Algorithm 1** and named task manager (TM). In TM, exploiting some thresholds, the contact can be detected effectively.

Algorithm 1 TM

Initialize $F_{T_H}, F_{T_L}, FI_{inx}$;
Input: F, FI_{inx};
If $(FI_{inx} \text{ is } 1 \text{ and } \|F\| > F_{T_H})$ **Then** $\psi = 1$; $\overline{S}_d = \overline{S}_{D_I}$; **Else** $\psi = 0$; $\overline{S}_d = \overline{S}_{D_F}$;
Return $\overline{S}_d, \psi$;

IV. HYBRID VISION/FORCE CONTROLLER DESIGN

In this section, FQSMC is designed to exploit a novel VGOSM for hybrid control of vision and force which leads to robustness against uncertainties and noises. It also can control the robot for both free-motion and hybrid vision/force tasks.

A. VARIABLE-GAIN ORTHOGONAL SLIDING MANIFOLD

1) ORTHOGONAL SLIDING MANIFOLD DESIGN
Consider the suggested sliding manifold $\sigma \in \mathbb{R}^6$ as follows:

$$
\sigma = \sigma_F + \sigma_s
\tag{32}
$$

where $\sigma_F \in R^6$ and $\sigma_s \in R^6$ are orthogonal vectors associated with the force error and the image feature error, respectively, presented as follows:

$$
\sigma_F = \mathbf{Q}e_F, \qquad \sigma_s = \mathbf{K}_c(\mathbf{I} - \mathbf{Q})e_P
\tag{33}
$$

where $e_F \in \mathbb{R}^6$, $e_p \in \mathbb{R}^6$, and $\mathbf{Q} \in \mathbb{R}^{6 \times 6}$ are the vectors of force and robot pose errors and the compliance selection matrix, respectively, presented in (34); $\mathbf{K}_c \in \mathbb{R}^{6 \times 6}$ is a positive definite

orthogonal matrix whose terms are variable, which will be discussed in the next subsection.

$$e_F = F - F_d, \quad e_P = \hat{\mathbf{L}}_s^{-1} e_s, \quad \mathbf{Q} = \psi D^T D, \quad e_s = S - S_d \quad (34)$$

where, $F_d \epsilon \mathbb{R}^6$ is the vector of desired forces, and $e_s \epsilon \mathbb{R}^6$ is the vector of image feature errors, $S_d \epsilon \mathbb{R}^6$ is the vector of desired image features, $D \epsilon \mathbb{R}^6$ is the selection vector whose entries are either zero or one, corresponding to directions where the exerted force must be controlled, ψ is zero when the robot has a free motion and one when the robot is interacting with the workpiece whose value is determined by the TM algorithm. In this research, the interaction force in the normal direction to the end-effector is controlled. Thus, D is defined as follows:

$$D = \begin{bmatrix} 0 & 0 & 1 & 0 & 0 & 0 \end{bmatrix} \quad (35)$$

In **Theorem 1**, it is proved that σ_F and σ_p are orthogonal. Hence, if $\lim\limits_{t \to +\infty} \sigma = 0$, then $\lim\limits_{t \to +\infty} \sigma_F = \lim\limits_{t \to +\infty} \sigma_s = 0$ i.e., the objective of the vision/force control is achieved.

Theorem 1: σ_F and σ_p vectors are orthogonal.

Proof: Consider the following relation:

$$\sigma_{FS} = \sigma_F \cdot \sigma_s = \sigma_F^T \sigma_s \quad (36)$$

where σ_{FP} is the results of dot-product of σ_F and σ_s. Substituting (33) into (36) yields:

$$\sigma_{FS} = (\mathbf{Q}e_F)^T (\mathbf{K}_c (\mathbf{I} - \mathbf{Q}) e_P) \quad (37)$$

Since $\mathrm{K_c}$ and Q are diagonal, (37) can be rewritten as:

$$\sigma_{FS} = e_F^T \mathbf{Q} (\mathbf{I} - \mathbf{Q}) \mathbf{K}_c e_P \quad (38)$$

In (38), $\mathbf{Q}^T (\mathbf{I} - \mathbf{Q}) = \mathbf{0}$, thus $\sigma_{FS} = 0$ Referring to [29], if the dot product of two vectors is zero, they are orthogonal, i.e., σ_F and σ_S are orthogonal and the proof is completed.

2) VARIABLE GAIN OF THE VISION TERM

One way to reduce the response time of IBVS is to increase the gain values in the control law. However, there is a limitation on this value because the high gain in IBVS controller tends to make the robotic system shaky and unstable. On the other hand, low gains may make the system very slow [18], [28]. To handle this issue, adaptive variable-gain IBVS and switch IBVS have been suggested, [18], [28], [39]. In the adaptive variable-gain method, the value of the control gain changes based on the norm of feature errors. When the norm is large, the gain sets to a large value to speed up the convergence rate. On the other hand, when the norm is small, the control gain is set to a small value to prevent unwanted oscillation and instability [28]. In the switch IBVS method, the visual motion is decomposed into translational and orientational motions of the camera, respectively. Then, each motion is controlled independently and with different feedback gains. However, due to the switching nature of this method, it is only applicable to vision control systems that are designed for regulation purposes [18]. Hence, it cannot be utilized in this study.

Based on the two mentioned methods, a novel variable gain using tangent hyperbolic function is developed for the vision term in the VGOSM. The continuous nature of the obtained method makes it possible to be adopted for vision systems with tracking trajectory purposes. In (33), $\mathbf{K}_c$ is identical to the feedback control gain of switch IBVS in [18] which is defined as $\mathbf{K}_C = \begin{bmatrix} \mathbf{K_t} & \mathbf{0}_{3 \times 3} \\ \mathbf{0}_{3 \times 3} & \mathbf{K_a} \end{bmatrix}$, where $\mathbf{K_t} \epsilon \mathbb{R}^{3 \times 3}$ and $\mathbf{K_a} \epsilon \mathbb{R}^{3 \times 3}$ are positive definite diagonal matrices of feedback gains associated with the translational and orientational motions of the camera, respectively. Also, translational and orientational errors of the camera motion are $e_{Pt} \epsilon \mathbb{R}^3$ and $e_{Pa} \epsilon \mathbb{R}^3$, respectively, determined as $e_P = \begin{bmatrix} e_{Pt}^T & e_{Pa}^T \end{bmatrix}^T$. Accordingly, the variable-gain relation is suggested as follows:

$$\mathbf{K_t} = \left(\frac{\tanh(a_t \|e_{Pt}\| + b_t) + 1}{2} \left(\mathbf{c}_{H_t} - \mathbf{c}_{L_t} \right) + \mathbf{c}_{L_t} \right) \mathbf{I_{3 \times 3}},$$

$$\mathbf{K_a} = \left(\frac{\tanh(a_a \|e_{Pa}\| + b_a) + 1}{2} \left(\mathbf{c}_{H_a} - \mathbf{c}_{L_a} \right) + \mathbf{c}_{L_a} \right) \mathbf{I_{3 \times 3}}$$

$$(39)$$

where a_t, a_a, b_t, and b_a are adjustable parameters that determine the characteristics of the smooth switching function $tanh(.)$. $\mathbf{c}_{H_t}$, $\mathbf{c}_{H_a}$, $\mathbf{c}_{L_t}$, and $\mathbf{c}_{L_t}$ are the lower and upper bounds of the feedback gains. The above equation aims to provide adjustable gains based on the error. According to this equation, it can be seen that as the error decreases, the gain values of K_t and K_a changes from their high-level values $\mathbf{c}_{H_t}$, $\mathbf{c}_{H_a}$ to their low-level values $\mathbf{c}_{L_t}$, and $\mathbf{c}_{L_a}$. As a result, the vision system converges fast when the error is high and avoids oscillation when the error is low.

B. FILTERED QUASI SLIDING MODE CONTROLLER

FQSMC not only is robust against uncertainties, but also filters out the noise in the feedback. It exploits a filter within its control law which is also considered in the procedure of its stability proof. Additionally, its continuous output leads to a chattering-free SMC. All of these features make FQSMC a candidate for the systems subject to large uncertainties and measurement noises such as the one in this study.

1) CONTROL LAW DESIGN

To derive the FQSMC control law, the time derivative of σ is taken. It results in appearing the system input, i.e., $u = \dot{q}$. Thus, $\dot{\sigma}$ is obtained as follows:

$$\dot{\sigma} = \mathbf{Q}\dot{e}_F + (\mathrm{diag}\{e_P\}(\mathbf{I} - \mathbf{Q})\mathbf{J}_K + \mathbf{K}_C(\mathbf{I} - \mathbf{Q}))\hat{\mathbf{L}}_s^{-1}\dot{e}_s \quad (40)$$

where $\mathbf{J}_K = \frac{\partial \mathrm{md}\{\mathbf{K}_C\}}{\partial e_P}$, in which md $\{\star\}$ is the function that takes a squared matrix $\star$ and returns its main diagonal as a vector. Taking time derivatives of (34) and then, substituting (6) and (9) into it, results in the following relations:

$$\dot{e}_F = \widehat{K}_f \hat{\mathbf{J}}_q u + \overline{\delta}_F - \dot{F}_d, \quad \dot{e}_s = \hat{\mathbf{L}}_s \hat{\mathbf{J}}_q u + \overline{\delta}_s - \dot{S}_d \quad (41)$$

Substituting (41) into (40) yields:

$$\dot{\sigma} = \mathbf{Q}\left(\widehat{K}_f \hat{\mathbf{J}}_q u - \dot{F}_d\right) + (\text{diag}\{e_P\}(\mathbf{I} - \mathbf{Q})\mathbf{J}_K$$
$$+ \mathbf{K}_C(\mathbf{I} - \mathbf{Q}))\hat{\mathbf{L}}_s^{-1}\left(\hat{\mathbf{L}}_s\hat{\mathbf{J}}_q u - \dot{\bar{S}}_d\right) + \delta_L \quad (42)$$

where

$$\delta_L = \mathbf{Q}\bar{\delta}_F + (\text{diag}\{e_P\}(\mathbf{I} - \mathbf{Q})\mathbf{J}_K + \mathbf{K}_C(\mathbf{I} - \mathbf{Q}))\hat{\mathbf{L}}_s^{-1}\bar{\delta}_s \quad (43)$$

Based on (42), the FQSMC law can be obtained as follows:

$$u = \left(\mathbf{Q}\widehat{K}_f\hat{\mathbf{J}}_q + (\text{diag}\{e_P\}(\mathbf{I} - \mathbf{Q})\mathbf{J}_K + \mathbf{K}_C(\mathbf{I} - \mathbf{Q}))\hat{\mathbf{J}}_q\right)^{-1}$$
$$\times \left(\eta + \mathbf{Q}\dot{F}_d + (\text{diag}\{e_P\}(\mathbf{I} - \mathbf{Q})\mathbf{J}_K\right.$$
$$\left. + \mathbf{K}_C(\mathbf{I} - \mathbf{Q}))\hat{\mathbf{L}}_s^{-1}\dot{\bar{S}}_d\right) \quad (44)$$

where

$$\begin{cases} \eta = -\mathbf{\Lambda_1}^{-1}\mathbf{\Lambda_3}\sigma_C - \mathbf{\Lambda_1}^{-1}\text{sat}\left(\boldsymbol{\phi}^{-1}\sigma_C\right) \\ \dot{\sigma}_C = -\mathbf{\Lambda_2}\sigma_C + \mathbf{\Lambda_1}\sigma \end{cases} \quad (45)$$

$$\text{sat}\left(\boldsymbol{\phi}^{-1}\sigma_C\right) = \begin{cases} \boldsymbol{\phi}^{-1}\sigma_C, & \left|\boldsymbol{\phi}^{-1}\sigma_C\right| < \mathbf{K} \\ \mathbf{K}\text{sign}\left(\boldsymbol{\phi}^{-1}\sigma_C\right), & \left|\boldsymbol{\phi}^{-1}\sigma_C\right| \geq \mathbf{K} \end{cases} \quad (46)$$

In (45) and (46), $\eta \epsilon \mathbb{R}^6$ is the reaching law and σ_C is the filtered value of σ; $\boldsymbol{\phi}\epsilon\mathbb{R}^{6\times6}$ is the positive definite orthogonal matrix of the boundary layer thickness; $\mathbf{K}\epsilon\mathbb{R}^6$ is the saturation threshold whose value is set based on the bounds of system uncertainties. The schematic of FGSMC is shown in FIGURE 6.
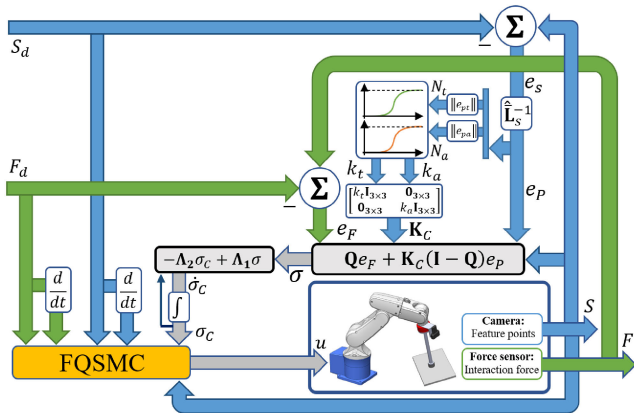

FIGURE 6. Schematic of the proposed robust hybrid controller.

2) STABILITY AND PERFORMANCE ANALYSIS
The stability proof of FQSMC is presented in **Theorem 2**. A necessary assumption for this theory is considered as follows:

Assumption 1: The following relation holds for δ_L:

$$|\delta_L| \leq D_L | D_L \epsilon \mathbb{R}^{6\times1}, \quad D_L > 0 \quad (47)$$

Theorem 2: Under the condition of (48), applying the FQSMC law of (44) to the dynamic system of (42) leads to its stability with a Quasi-sliding motion, i.e., $|\sigma| < \delta_B$ for all $t \geq T_r$ where $\delta_B, \epsilon_\sigma > 0$ and $T_r > 0$ [21], provided that **Assumption 1** is satisfied.

$$\mathbf{\Lambda_1}, \mathbf{\Lambda_2}, \mathbf{\Lambda_3} > 0, \quad \mathbf{K} > \mathbf{\Lambda_1}D_L,$$
$$(\mathbf{\Lambda_2} - \omega\mathbf{I}) > \mathbf{0},$$
$$\sqrt{2}(\mathbf{\Lambda_2} - \omega\mathbf{I})^{\frac{1}{2}}\sqrt{2\omega}\mathbf{\Lambda_3}^{\frac{1}{2}} \geq |(\gamma\mathbf{I} - \omega\mathbf{\Lambda_2} - \mathbf{\Lambda_3})| + 2\boldsymbol{\phi},$$
$$\mathbf{\Lambda_2^2} - 4\left(\mathbf{\Lambda_3} + \boldsymbol{\phi}^{-1}\right) \geq 0, \quad 0 < \omega < 1, \quad \gamma > 1 \quad (48)$$

Proof: Substituting (44) into (42) yields:

$$\begin{cases} \dot{\sigma} = -\mathbf{\Lambda_1}^{-1}\mathbf{\Lambda_3}\sigma_C - \mathbf{\Lambda_1}^{-1}\text{sat}\left(\boldsymbol{\phi}^{-1}\sigma_C\right) + \delta_L \\ \dot{\sigma}_C = -\mathbf{\Lambda_2}\sigma_C + \mathbf{\Lambda_1}\sigma \end{cases} \quad (49)$$

By taking the time derivative of the second row of (49) and substituting it into its first row, the following relation is obtained:

$$\ddot{\sigma}_C = -\mathbf{\Lambda_2}\dot{\sigma}_C - \mathbf{\Lambda_3}\sigma_C\text{-sat}\left(\boldsymbol{\phi}^{-1}\sigma_C\right) + \mathbf{\Lambda_1}\delta_L \quad (50)$$

Consider the following candidate Lyapunov function:

$$V = \gamma\sigma_C^T\sigma_C + 2\omega\sigma_C^T\dot{\sigma}_C + \dot{\sigma}_C^T\dot{\sigma}_C \quad (51)$$

Based on (48), it can be deduced that $\omega < \gamma^{1/2}$. This inequality results in the following relation:

$$\left|2\omega\sigma_C^T\dot{\sigma}_C\right| \leq \left|2\gamma^{\frac{1}{2}}\sigma_C^T\dot{\sigma}_C\right|, \quad \left|\gamma\sigma_C^T\sigma_C\right| \geq 0, \left|\dot{\sigma}_C^T\dot{\sigma}_C\right| \geq 0 \quad (52)$$

Additionally, the following relation holds:

$$\left(\gamma^{\frac{1}{2}}\sigma_c + \dot{\sigma}_c\right)^T\left(\gamma^{\frac{1}{2}}\sigma_c + \dot{\sigma}_c\right)$$
$$= \gamma\sigma_C^T\sigma_C + 2\gamma^{\frac{1}{2}}\sigma_C^T\dot{\sigma}_C + \dot{\sigma}_C^T\dot{\sigma}_C \geq 0 \quad (53)$$

By comparing (52) with (53), it can be deduced that $\gamma\sigma_C^T\sigma_C + 2\omega\sigma_C^T\dot{\sigma}_C + \dot{\sigma}_C^T\dot{\sigma}_C = V = 0$ when $(\sigma_C, \dot{\sigma}_C) = (0, 0)$ and $V > 0$ when $(\sigma_C, \dot{\sigma}_C) \neq (0, 0)$: the required condition of a Lyapunov function [20], [21]. $\dot{V}$ is obtained as follows:

$$\dot{V} = 2\gamma\sigma_C^T\dot{\sigma}_C + 2\omega\dot{\sigma}_C^T\dot{\sigma}_C + 2\omega\sigma_C^T\ddot{\sigma}_C + 2\dot{\sigma}_C^T\ddot{\sigma}_C \quad (54)$$

To prove the Quasi SMC under the proposed control law, the attraction towards the boundary layer should be illustrated, i.e., when $\left|\boldsymbol{\phi}^{-1}\sigma_C\right| \geq \mathbf{K}$, $\dot{V} < 0$. Substituting (50) into (54) yields:

$$\dot{V} = \dot{\sigma}_c^T\left(2\left(\gamma\mathbf{I} - \omega\mathbf{\Lambda_2} - \mathbf{\Lambda_3}\right)\sigma_c - 2\left(\mathbf{K}\text{sign}\left(\sigma_C\right) - \mathbf{\Lambda_1}\delta_L\right)\right)$$
$$- 2\dot{\sigma}_c^T\left(\mathbf{\Lambda_2} - \omega\mathbf{I}\right)\dot{\sigma}_C - 2\omega\sigma_c^T\mathbf{\Lambda_3}\sigma_C - 2\omega\sigma_c^T$$
$$\times \left(\mathbf{K}\text{sign}\left(\sigma_C\right) - \mathbf{\Lambda_1}\delta_L\right) \quad (55)$$

Based on **Assumption 1** and (48), the following relations yield:

$$-2\omega\sigma_c^T\left(\mathbf{K}\text{sign}\left(\sigma_C\right) - \mathbf{\Lambda_1}\delta_L\right) \leq 0 \quad (56)$$

$$\sqrt{2}\,(\mathbf{\Lambda_2}-\omega\mathbf{I})^{\frac{1}{2}}\,\sqrt{2\omega}\mathbf{\Lambda_3^{\frac{1}{2}}}$$

$$\geq |(\gamma\mathbf{I}-\omega\mathbf{\Lambda_2}-\mathbf{\Lambda_3})|+2\boldsymbol{\phi}$$

$$\geq \left| \left((\gamma\mathbf{I}-\omega\mathbf{\Lambda_2}-\mathbf{\Lambda_3})-\left(\frac{\mathbf{K}}{|\sigma_C|}-\frac{\mathbf{\Lambda_1}\delta_L}{|\sigma_C|}\right)\right) \right| \quad (57)$$

Comparing (56) and (57) with (55) yields:

$$\dot{V} < -2\left((\mathbf{\Lambda_2}-\omega\mathbf{I})^{\frac{1}{2}}\dot{\sigma}_c+\sqrt{\omega}\mathbf{\Lambda_3^{\frac{1}{2}}}\sigma_c\right)^{\mathrm{T}}$$

$$\times \left((\mathbf{\Lambda_2}-\omega\mathbf{I})^{\frac{1}{2}}\dot{\sigma}_c+\sqrt{\omega}\mathbf{\Lambda_3^{\frac{1}{2}}}\sigma_c\right) \quad (58)$$

Accordingly, when $\left|\boldsymbol{\phi}^{-1}\sigma_C\right| \geq \mathbf{K}$, one has $\dot{V} < 0$.

When $\left|\boldsymbol{\phi}^{-1}\sigma_C\right| < \mathbf{K}$, (50) is obtained as:

$$\ddot{\sigma}_C = -\mathbf{\Lambda_2}\dot{\sigma}_C-(\mathbf{\Lambda_3}+\boldsymbol{\phi}^{-1})\sigma_C+\mathbf{\Lambda_1}\delta_L \quad (59)$$

Since Λ_1 to Λ_3 and Φ are constants, the relation above can be transformed to the frequency domain using Laplace transformation as follows:

$$\Sigma_c p^2 + \mathbf{\Lambda_2}\Sigma_c p + \left(\mathbf{\Lambda_3}+\boldsymbol{\phi}^{-1}\right)\Sigma_c = \mathbf{\Lambda_1}\Delta_{\mathrm{L}} \quad (60)$$

where p is Laplace operator, $\Sigma_c = \mathcal{L}\{\sigma_c\}$ and $\Delta_{\mathrm{L}} = \mathcal{L}\{\delta_L\}$, where $\mathcal{L}\{\star\}$ is Laplace function. Thus, the transfer function $\mathrm{T}_1(p) = \Sigma_c\Delta_{\mathrm{L}}^{-1}$ is obtained as:

$$\mathrm{T}_1(p) = \Sigma_c\Delta_L^{-1} = \mathbf{\Lambda_1}\left((p\mathbf{I}+\mathbf{R_1})(p\mathbf{I}+\mathbf{R_2})\right)^{-1},$$

$$\mathbf{R_1} = \frac{1}{2}\left(-\mathbf{\Lambda_2}+\left(\mathbf{\Lambda_2^2}-4\left(\mathbf{\Lambda_3}+\boldsymbol{\phi}^{-1}\right)\right)^{1/2}\right),$$

$$\mathbf{R_2} = \frac{1}{2}\left(-\mathbf{\Lambda_2}-\left(\mathbf{\Lambda_2^2}-4\left(\mathbf{\Lambda_3}+\boldsymbol{\phi}^{-1}\right)\right)^{1/2}\right) \quad (61)$$

Based on (48), (61) has real poles. Also, taking Laplace of the second row of (49) results in the following transfer function:

$$\mathrm{T}_2(p) = \Sigma_c\Sigma^{-1} = (p\mathbf{I}+\mathbf{\Lambda_2})^{-1}\mathbf{\Lambda_1} \quad (62)$$

where $\Sigma = \mathcal{L}\{\sigma\}$. Based on (48), (61), and (62) $\mathrm{T}_3(p) = \Sigma\Delta_{\mathrm{L}}^{-1}$ can be obtained as follows:

$$\mathrm{T}_3(p) = \mathrm{T}_1(p)\,\mathrm{T}_2^{-1}(p)$$

$$= \mathbf{\Lambda_1}\left((p\mathbf{I}+\mathbf{\Lambda_2})(p\mathbf{I}+\mathbf{R_1})(p\mathbf{I}+\mathbf{R_2})\right)^{-1} \quad (63)$$

Based on (48), the nominator's coefficients of $\mathrm{T}_3(p)$ are positive and real (there is not nay imaginary roots). Hence, it is stable. So, it can be seen that the response has its maximum magnitude in zero frequency [14]. It means that the response is bounded as $|\sigma| < \delta_B$ where $\delta_B = \mathrm{T}_3(0) = (\mathbf{R_1})^{-1}(\mathbf{R_2})^{-1}\mathbf{\Lambda_1}(\mathbf{\Lambda_2})^{-1} = \mathbf{\Lambda_1^2}\left(\mathbf{\Lambda_3}+\boldsymbol{\phi}^{-1}\right)^{-1}\mathbf{\Lambda_2^{-1}}$. Thus, FQMC is a Quasi SMC and the theorem is proved.

Remark 1: T_2 (p) in (62) is a low-pass filter that exists in the reaching law in (45). Thus, it filters out the existing noises in the orthogonal sliding manifold σ emanated from force sensor and camera measurement noises. Also, FQSMC does not exploit a discontinuous switching function in the control law, it is free of chattering.

Remark 2: Typically, in Quasi SMC, there is a trade-off between the tracking error and chattering. Hence, if the control gains are set to large values, chattering increases due

to the existing noises in the sensors' feedback. If they are set to small values, the tracking error may increase. However, in FQSMC, the intrinsic filter smooths the signals and thus the controller gains can be set to larger values. Consequently, the tracking precision will increase without generating adverse chattering.

V. EXPERIMENTAL RESULTS AND DISCUSSION
In this section, several experiments have been conducted to investigate the performance and feasibility of the proposed method.

A. EXPERIMENTAL SETUP
The setup consists of a six-DOF DENSO VP6242G robot, a Quanser open architecture control module, a Logitech C270 digital camera with an EIH configuration, a six-axis ATI model 200 industrial automation force sensor installed on the robot end-effector. MATLAB©2011-b software is employed for implementing the proposed methods. In the tests, the control process sampling time is set to $1/29$s. The setup components are shown in FIGURE 7.a. The values of the physical parameters of the DENSO-VP6242G robot and the camera are available in [18]. To show the impact of the robot kinematic uncertainties on the control process, a slight change, around 5%, is applied to these values. To extract the image features to be used in IBVS, a red rectangular object is mounted on the workpiece. Note that two workpieces with planar and curved surfaces are provided for the tests (FIGURE 7.b and c). The constraint relations of the work-pieces' surfaces are as follows:

$$\begin{aligned}\text{Planar}: \quad & \mathrm{f}_S\,(x,y,z)=z,\\ \text{Curved}: \quad & \mathrm{f}_S\,(x,y,z)=(z-0.15)^2+x^2-0.15^2\end{aligned} \quad (64)$$

The camera captures the object. Then, by processing the captured image, the edges of the rectangular object are detected as the four feature points (FIGURE 7.a- top-right).
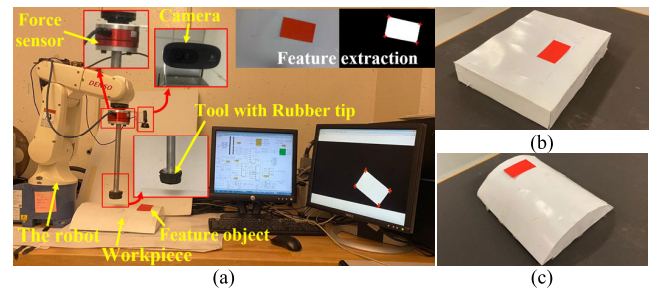

FIGURE 7. (a) Experimental setup. (b) Planar workpiece. (c) Curved workpiece.

B. RESULT OF TRAINING THE NEURAL NETWORK
To train the NN, n_d is set to 1000 and 20% of the sampling data is considered for the validation test. The maximum number of iterations for training is set to 1000. FIGURE 8 shows the results of training the NN for the planar work-piece. The cost value for training data has converged to zero after twenty iterations which means the NN is trained well.

Additionally, the cost value for validation data shows a consistent decrement which means the NN is not over-trained.
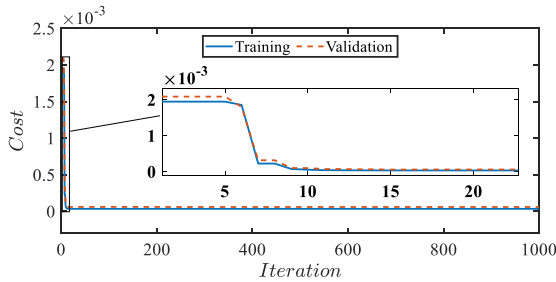

FIGURE 8. Training the NN.

C. TUNING THE CONTROLLERS' PARAMETERS

To compare the performance of the proposed controller to other traditional well-known methods, P/PI (proportional controller for vision part and proportional-integral controller for interaction force part) and traditional SMC are also considered to be applied to the robot. Note that to have a fair comparison, the controller parameters must be tuned properly before applying to the system.

In this study, the optimal tuning method presented in [20] is employed for the gain tuning of the controllers. In this method, first, the closed-loop system is modeled using the proposed control method. Then, a cost function is defined comprising of several objective functions associated with the reaching time, chattering level, control effort, sliding variable value, and tracking error. Finally, MTOA is used to solve the optimization problem, whose solution is the set of optimally tuned parameters of the controller [20]. The main advantage of this tuning method is that it results in the optimality of the controller not only for a specific path but also for any arbitrary desired path. The nonlinear terms of the controller also contain the desired signals that are not considered in the optimization, and only the terms that are directly influenced by the controller gains are considered.

Such a tuning method not only results in an optimal control process but also provides a fair comparison between the proposed controller and other designated approaches. FIGURE 9 illustrates the results of the optimization process for P/PI, SMC, and FQSMC. Referring to this figure, the best and average cost values have converged to the minimum values (i.e., 0.25, 0.52, and 0.09, for P/PI, SMC, and QSMC, respectively) after at least 130 iterations. However, the minimum cost value for SMC is higher than that for P/PI. Also, the minimum cost value for P/PI is higher than that for FQSMC. The reason is that the existing filter in FQSMC allows the optimization algorithm to set the controller gains to higher values. Consequently, higher precision and lower control effort will be achieved. Furthermore, the existence of the variable gain in FQSMC results in more flexibility and hence lower cost value. However, for SMC and P/PI, setting higher controller gains for increasing the precision result in amplifying the noise which will appear in the

controller output. The chattering problem in SMC results in a higher level of control effort and thus its cost value is even higher than that of the P/PI.
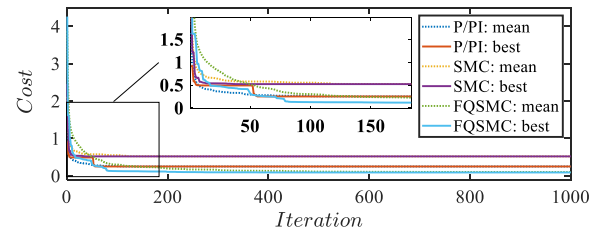

FIGURE 9. Gain tuning using the method suggested in [20].

D. DESIGN OF THE EXPERIMENTAL TESTS

For the experiments, five experimental tests are designed. In the first four tests, the performance of the proposed MAPF-CGTSP method and switching between the free-motion and interacting with the workpiece, along with the proposed controller is investigated for the environments with obstacles. To this end, four operations labeled as Op.1,..., Op.4 are considered with a different configuration of the number of tasks and the obstacle positions to analyze the performance and accuracy of the proposed task-sequence/path planning using MTOA in challenging situations. The environment configurations corresponding to each operation are depicted in the next subsection. The equations Obstacles and tasks of Op.1 to Op.4 are given in (65).

$$OP.1:$$

$$\text{Task 1:} \begin{cases} \text{Type:2} \\ P_{wd}(\vartheta) = \begin{bmatrix} 0.04\cos((\vartheta 1.6 - 0.3)\pi) \\ 0.02\sin((3.2\vartheta - 0.6)\pi) + .1 \\ 0 \end{bmatrix} \\ v_d = 0.001 \\ F_d(\vartheta) = 8, \end{cases}$$

$$\text{Task 2:} \begin{cases} \text{Type:1} \\ P_{wd}(\vartheta) = \begin{bmatrix} .02 & .1 & 0 \end{bmatrix}^{\text{T}} \\ T_t = 50 \\ F_d(\vartheta) = 8, \end{cases}$$

$$\text{Task 3:} \begin{cases} \text{Type:1} \\ P_{wd}(\vartheta) = \begin{bmatrix} -.02 & .1 & 0 \end{bmatrix}^{\text{T}} \\ T_t = 30 \\ F_d(\vartheta) = 8 \end{cases},$$

$$\text{Task 4:} \begin{cases} \text{Type:2} \\ P_{wd}(\vartheta) = \begin{bmatrix} 0.08\cos\left(\frac{1}{3}\vartheta\pi + \frac{\pi}{3}\right) \\ 0.08\sin\left(\frac{1}{3}\vartheta\pi + \frac{\pi}{3}\right) + 0.1 \\ 0 \end{bmatrix} \\ v_d = 0.001 \\ F_d(\vartheta) = 8 \end{cases}$$

No obstacle.

OP.2 :

$$\text{Task 1:} \begin{cases} \text{Type:2} \\ P_{wd}(\vartheta) = \begin{bmatrix} 0.02\vartheta - .06 \\ 0.1 \\ 0 \end{bmatrix}, \\ v_d = 0.0005 \\ F_d(\vartheta) = 8 \end{cases}$$

$$\text{Task 2:} \begin{cases} \text{Type:1} \\ P_{wd}(\vartheta) = \begin{bmatrix} 0.07 & 0.12 & 0 \end{bmatrix}^{\text{T}} \\ T_t = 30 \\ F_d(\vartheta) = 8, \end{cases}$$

$$\text{Task 3:} \begin{cases} \text{Type:2} \\ P_{wd}(\vartheta) = \begin{bmatrix} 0.07 \\ 0.07 & 0.14 & 0 \\ 0.01045 \end{bmatrix}^{\text{T}} \\ v_d = 0.0005 \\ F_d(\vartheta) = 8, \end{cases}$$

Two obstacles

OP.3 :

$$\text{Task 1:} \begin{cases} \text{Type:2} \\ P_{wd}(\vartheta) = \begin{bmatrix} 0.055 \\ 0.111 - .03\vartheta \\ -.01045 \end{bmatrix} \\ v_d = 0.0005 \\ F_d(\vartheta) = 8, \end{cases}$$

$$\text{Task 2:} \begin{cases} \text{Type:1} \\ P_{wd}(\vartheta) = \begin{bmatrix} -.055 & 0.111 & -.01045 \end{bmatrix}^{\text{T}} \\ T_t = 30 \\ F_d(\vartheta) = 8 \end{cases}$$

One obstacle

OP.4 :

$$\text{Task 1:} \begin{cases} \text{Type:2} \\ P_{wd}(\vartheta) = \begin{bmatrix} .02\sin\left(\frac{1}{2}\vartheta\pi + \frac{\pi}{2}\right) + .03 \\ .02\cos\left(\frac{1}{2}\vartheta\pi + \frac{\pi}{2}\right) + .125 \\ \left(.15^2 - \left(\left(.02\sin\left(\frac{1}{2}\vartheta\pi + \frac{\pi}{2}\right) \\ + .03\right)\right)^2\right)^{.5} - .15 \end{bmatrix} \\ v_d = 0.001 \\ F_d(\vartheta) = 8, \end{cases}$$

$$\text{Task 2:} \begin{cases} \text{Type:1} \\ P_{wd}(\vartheta) = \begin{bmatrix} -.055 & .111 & -0.01045 \end{bmatrix}^{\text{T}} \\ T_t = 50 \\ F_d(\vartheta) = 8 \end{cases}$$

Two obstacles (65)

The objective of the fifth test is to evaluate the performance of the proposed hybrid control method and compare the results with other aforementioned well-known schemes in terms of tracking error, convergence rate, control effort, and chattering level. An infinity-shaped path on the planar workpiece is defined as the desired path and a sinusoidal desired signal is defined as the desired interaction force as:

$$P_d(t) = [\,0.05\cos(0.025t) + 0.02 \quad 0.025\sin(0.05t) \quad 0$$
$$0 \quad 0 \quad 0\,]^{\text{T}}, \quad F_d(t) = 1.5\sin(0.15t) + 6 \tag{66}$$

E. RESULTS AND DISCUSSION OF THE EXPERIMENTAL TESTS

1) HYBRID TASK SEQUENCE/PATH PLANNING (TESTS 1 TO 4)

In these tests, a set of four operations is presented. The performance of the proposed optimal task sequence/path planning method using the MAPF strategy is compared to that of the traditional APF. Furthermore, a comparative study of solving the MAPF-CGTSP by the mix-integer MTOA against the PSO, GWO, membrane-inspired evolutionary algorithm (memE) is presented to compare the performance of the proposed optimization algorithm. Please note that the parameters of the optimization algorithms are set in a way that their overall populations are almost 10, 20, 20, and 20 for Op. 1 to Op.4, respectively.

As mentioned before, this problem is composed of two various problems including finding the optimal task sequence and also the parameters of the proposed MAPF method to have an optimal collision-free path between the tasks. In the first row of TABLE 1, the result of solving the task sequence part of the optimization problem for each operation, using the MTOA, and the direction of Type 2 tasks is listed in two different subsets. For each case, MTOA is executed thirty times (30 independent runs) to reach the solution. The first subset defines the sequence of the tasks for each operation and the second subset shows the direction of entering to a Type 2 task and exiting from it. Note that, in the second subset, 0 is corresponding to the endpoint A for a Type 2 task and 1 is corresponding to the endpoint B. The other parameters listed in TABLE 1 are obtained by MTOA for the MAPF to reach an optimized collision-free path between the tasks while the sequence of the starting and ending points of each path has already been obtained.

Based on this table, in the first operation, four different tasks, two Type 2 tasks and two Type 1 tasks, are defined on a planar workpiece. Based on the optimal task sequences of

TABLE 1. The optimized parameters for MAPF-CGTSP using MTOA.

Optimization Parameters	Op. 1	Op. 2	Op. 3	Op. 4
Task seq.	{2 1 3 4}|{01}	{2 3 1}|{1}	{1 2}|{0}	{1 2}|{0}
k_a	N/A	0.8234	0.2079	0.4241
k_r	N/A	0.3735	0.9341	0.0603
α_p	N/A	0.7738	0.4106	0.7269
α_{rot}	N/A	0.000002638	0.00000941	0
ρ_0	N/A	0.5163	0.3707	0.9486
k_{r_1}	N/A	0.008908	0.1567	0.8594
α_{p_1}	N/A	0.9204	0.5168	0.002304
α_{rot_1}	N/A	0.3504	0.00001312	0.4614
ρ_{0_1}	N/A	0.9654	0.8814	0.3977
k_{r_2}	N/A	0.2847	N/A	0.4181
α_{p_2}	N/A	0.5363	N/A	0.8311
α_{rot_2}	N/A	0.000008907	N/A	0.5818
ρ_{0_2}	N/A	0.3105	N/A	0.01136

FIGURE 10. Op. 1-Desired paths and points of four tasks on the workpiece.

FIGURE 11. The robot operating Op. 1.

the first operation, it can be observed that this operation starts with the second task (T2) which is a Type 1 task or a point and moves towards the first task (T1) which is a Type 2 task or a path. The direction of Type 2 tasks affects achieving an optimal general path for the operations. Based on the obtained direction for the Type 2 tasks in this table, the first Type 2 task (T1) starts from the end-point A (T1A) and exits from the endpoint B (T1B). Then, the robot moves to the third task (T3) which is the other Type 1 task. Finally, the robot moves towards the last one which is the fourth task (T4). This task is also a Type 2 task with two endpoints which based on the second element of the second subset, the robot will enter from its endpoint B (T4B). The desired tasks and the paths between each two tasks are depicted in FIGURE 10. From this figure, it can be seen that the first operation is free of obstacles. Therefore, the path between the tasks can be considered as a straight line. Hence, this operation does not require to use MAPF for obtaining the path between the tasks. The robot carrying out the tasks for the first operation is shown in FIGURE 11. The results of the vision/force control system in performing the first operation are presented in FIGURE 12.a and b. According to FIGURE 12.a, which shows the trajectory tracking of Op. 1 on the image plane, it can be seen that the robot tracks the two paths and regulates on each point of the tasks one-by-one until the entire operation is done. Referring to FIGURE 12.b, the effectiveness of the force control process for each task and also the feasibility of the proposed method for switching between the free motion and interaction with the workpiece is demonstrated.

In the second operation, three different tasks, a Type 2 task and two Type 1 tasks, are defined on a planar workpiece. Based on the optimal task sequences of the second operation, the robot performs the whole operation. The desired tasks and the paths between each two tasks which are obtained by APF and MAPF methods are depicted in FIGURE 13.a and b, respectively. From these figures, it can be observed that two obstacles are placed between three defined tasks. In FIGURE 13.a, using the APF method, the
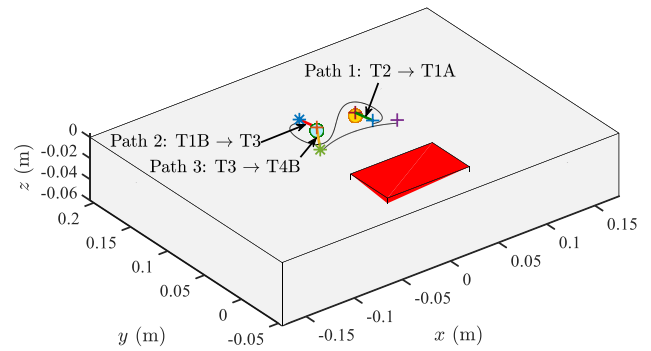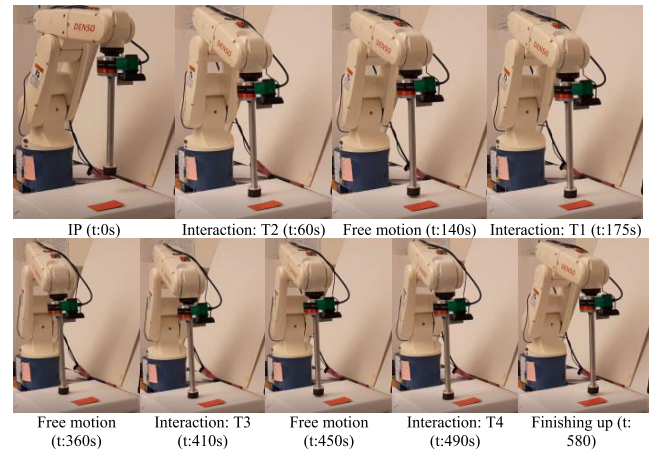
robot moves from the NAEP towards the AEP of the first task sequence selected by MTOA (T2) through Path 1. Then, using APF method, the robot moves from T2 to T3 (the second task sequence selected by MTOA) through Path 2 which is depicted in FIGURE 13.a. However, the APF method does not work properly in reaching the third task sequence (T1). Hence, the robot will be trapped and could not continue its trajectory to reach the target. FIGURE 13.b shows that when using the MAPF method, the robot successfully reaches the target. So, the proposed method outperforms the traditional APF method, since it gives a minimum collision-free traveled distance in performing this multi-task operation in presence of obstacles. The robot carrying out the tasks for the second operation using MAPF is shown in FIGURE 14. The results of the vision/force control system in performing the second operation are presented in FIGURE 15.a and b. According to FIGURE 15.a, which shows the trajectory tracking of Op. 2 on the image plane, it can be seen that the robot tracks the defined path and regulates on each point of the tasks one-by-one until the entire operation is done. Referring to FIGURE 15.b, the effectiveness of the force control process for each task and also the feasibility of the proposed method for switching between the free motion and interaction with the workpiece is demonstrated.
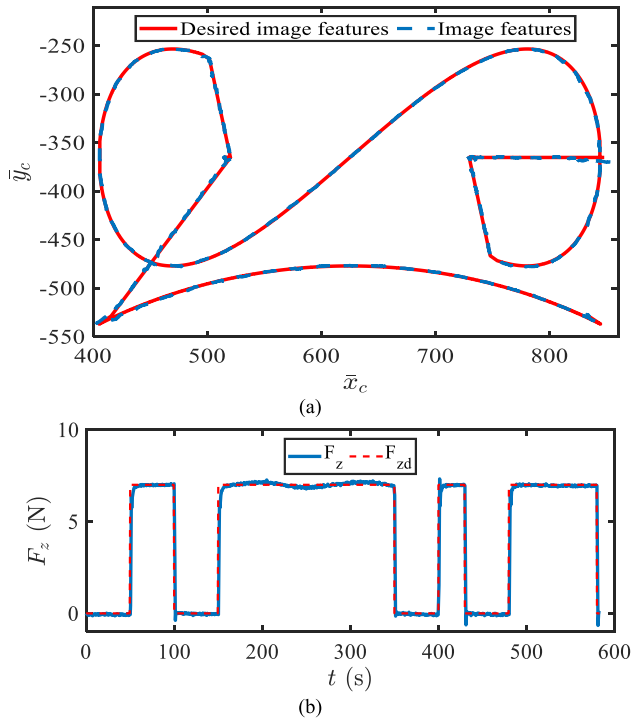
FIGURE 12. Path tracking in the image space and force control of all the tasks of OP. 1. (a) Tracking the paths and points in the image space of Op. 1. (b) Controlling the force of Op. 1.

In the third operation, two different tasks, a Type 2 task and two Type 1 tasks, are defined on a curved workpiece to show the effectiveness of the proposed method in performing the multi-task operation on more complicated workpieces. Based on the optimal task sequences of the third operation, the robot performs the whole operation. The desired tasks and the paths between each two tasks which are obtained by APF and MAPF methods are depicted in FIGURE 16, respectively. From these figures, it can be observed that one obstacle is placed between two defined tasks. In FIGURE 16.a, using the APF method, the robot moves from the NAEP towards the AEP of the first task sequence selected by MTOA (T1) through Path 1. After completing T1, the robot is required to move towards the other task (T2) from the other endpoint of the first task (T1B).

However, the APF method does not work properly in reaching T2. Hence, the robot will be trapped and could not continue its trajectory to reach the target. FIGURE 16.b shows that when using the MAPF method, the robot successfully reached the target. So, the proposed method outperforms the traditional APF method, since it gives a minimum collision-free traveled distance in performing this multi-task operation in presence of obstacles. The robot carrying out the tasks for the third operation is shown in FIGURE 17. The results of the vision/force control system in performing the third operation are presented in FIGURE 18. According to FIGURE 18.a, which shows the trajectory tracking of Op. 3 on the image plane, it can be seen that the robot tracks the defined path and regulates the desired point of the task until the entire operation
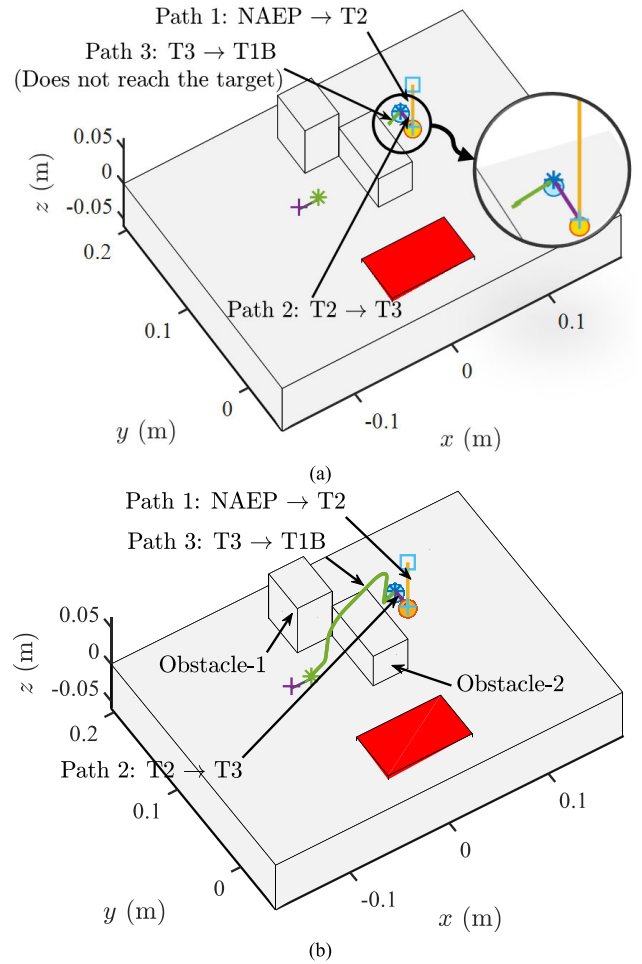

FIGURE 13. Op. 2 (a) Desired paths and points of three tasks on the workpiece using APF method. (b) Desired paths and points of three tasks on the workpiece using MAPF method.
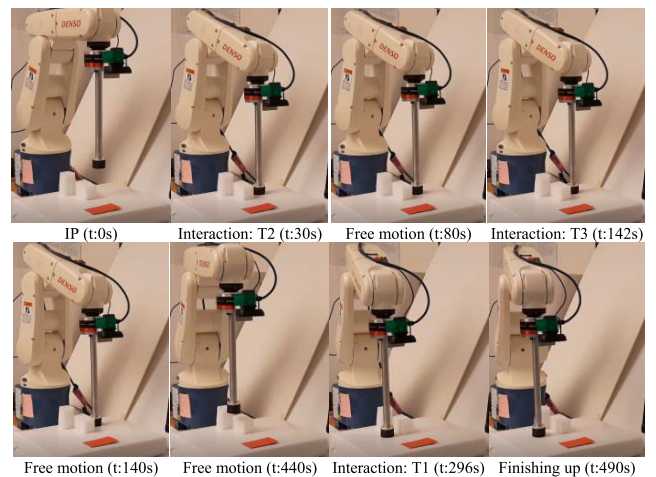

FIGURE 14. The robot operating Op. 2.

is done. Referring to FIGURE 18.b, the effectiveness of the force control process for each task and also the feasibility of the proposed method for switching between the free motion and interaction with the workpiece is demonstrated.
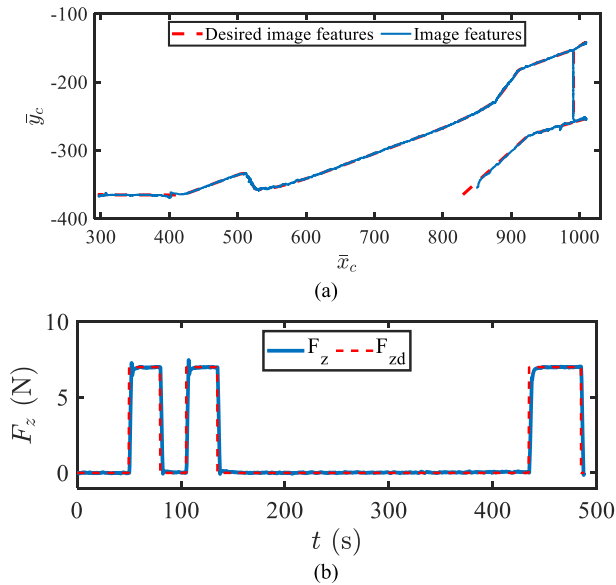
FIGURE 15. Path tracking in the image space and force control of all the tasks of OP. 2. (a) Tracking the paths and points in the image space of Op. 1. (b) Controlling the force of Op. 2.

The fourth operation is also accomplished on a curved surface with a different obstacle configuration. Two different tasks are defined for this operation. The results obtained in FIGURE 19.a and b, show that the APF method cannot finish the operation successfully. However, using the MAPF method, the operation is performed properly. The robot carrying out the tasks for the fourth operation is shown in FIGURE 20.

The results of the control process for the intended tasks are presented in FIGURE 21. According to FIGURE 21.a, the robot has tracked the desired features for each task when interacting with the workpiece and between the tasks by free-motion properly to complete the operation. Referring to FIGURE 21.b, it can be seen that the interacting force is controlled properly as well. These results show not only the effectiveness of the proposed path/task sequence planning, but also the feasibility of the proposed hybrid control method for different workpieces.

Each test was independently executed 30 times for each operation. The results provided in TABLE 2., show the arithmetic best, mean, worst, and standard deviation of the path length in the image plane for the 30 individual tests on each operation. From this table, it can be concluded that the MTOA method outperforms the other optimization algorithms. The best path obtained using the MTOA for the first operation is the same as the other methods, since the environment is free of obstacles which leads to a simple CGTSP problem. Therefore, in this operation, the optimization problem converts to a simple problem of finding the integer sequence of the tasks which is obvious that all provided algorithms have successfully reached the desired sequence to minimize the path length. For the other operations, it can be observed that the MTOA method overcomes the drawback of PSO
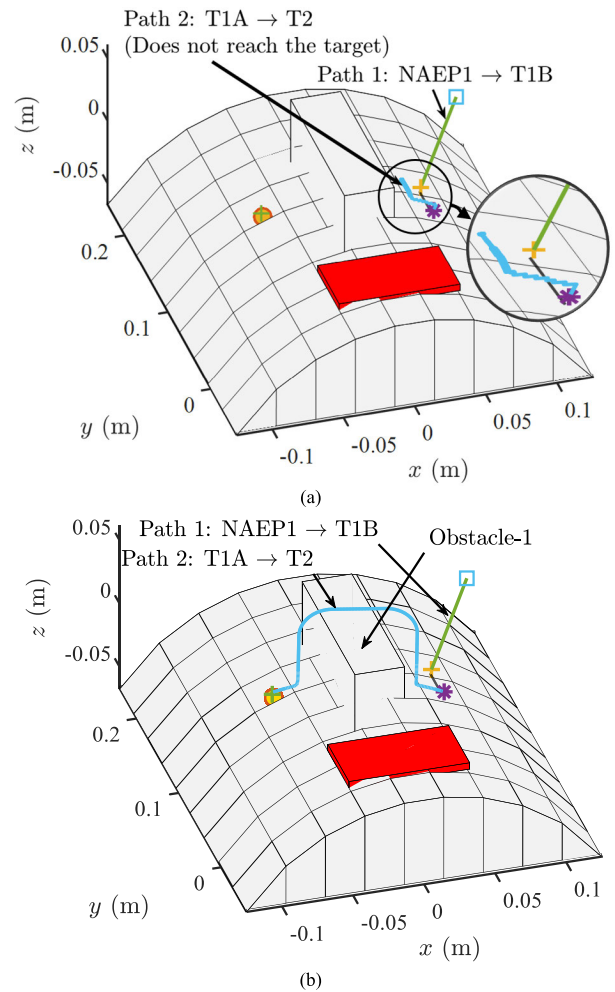

FIGURE 16. Op. 3 (a) Desired paths and points of two tasks on the workpiece using APF method. (b) Desired paths and points of two tasks on the workpiece using MAPF method.
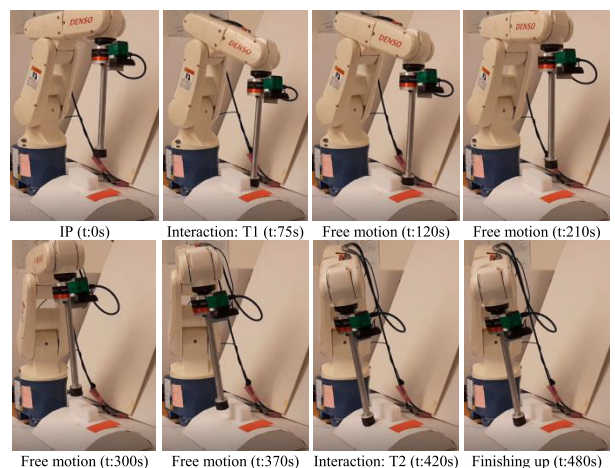

FIGURE 17. The robot operating Op. 3.

and GWO which are easy to be trapped into local optimum on average. The result also tells that MTOA has a better performance than memE in dealing with environments with obstacles.
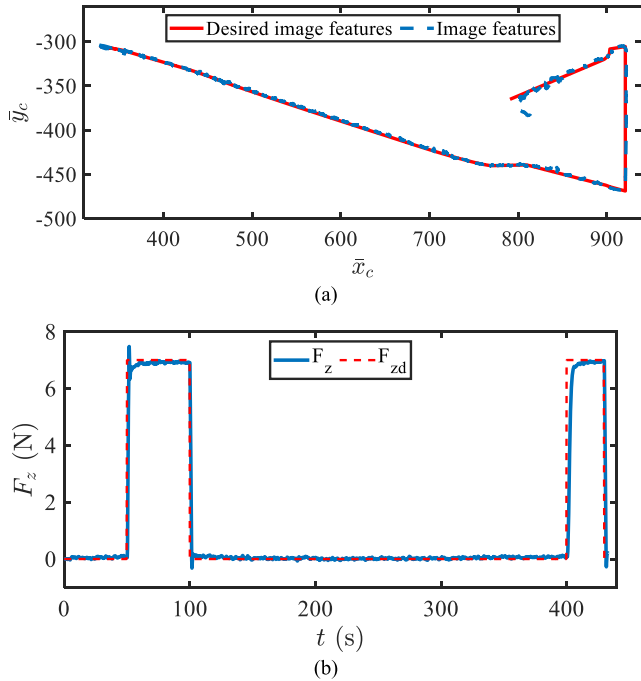
(a)

(b)

FIGURE 18. Path tracking in the image space and force control of all the tasks of OP. 3. (a) Tracking the paths and points in the image space of Op. 1. (b) Controlling the force of Op. 3.

TABLE 2. Results of the different optimization algorithms for all operations.

Operation	Statistics	PSO	GWO	memE	MTOA
Op. 1	Best	0.4803	0.4803	0.4803	0.4803
	Mean	0.5415	0.4843	0.4803	0.4803
	Worst	0.7406	0.5492	0.4803	0.4803
	Std.	0.07183	0.01533	0	0
Op. 2	Best	1.1909	1.1733	1.172	1.169
	Mean	20176.93	11000.733	1.2107	1.2015
	Worst	73333.70	36667.033	1.4710	1.396
	Std.	22182.96	17238.83	0.07289	00.05903
Op. 3	Best	1.175	1.172	1.171	1.167
	Mean	1834.8	1.174	1.175	1.172
	Worst	36667.03	1.213	1.209	1.201
	Std.	8198.66	0.01155	0.01068	9.9476e-3
Op. 4	Best	0.6985	0.6974	0.6948	0.6937
	Mean	5501.1	3667.76	0.6959	0.6941
	Worst	36667.03	36666.6	0.6974	0.6974
	Std.	13432.1	11285.26	0.014751	1.1282e-03

FIGURE 22 provides a graphical summary of the improvement percentage of the task sequence/path planning results in terms of path length for the methods GWO, MemE, and MTOA compared to the PSO. The result in this figure shows that solving the MAPF-CGTSP using MTOA method provides the highest improvement percentage compared to the other methods.

2) TEST 5: COMPARISON OF THE PERFORMANCE OF THE PROPOSED HYBRID CONTROLLER TO OTHER WELL-KNOWN METHODS

Using NN_{sd} in (28), the desired image feature signal of the second test (FIGURE 23.a) can be extracted as illustrated in FIGURE 23.b.
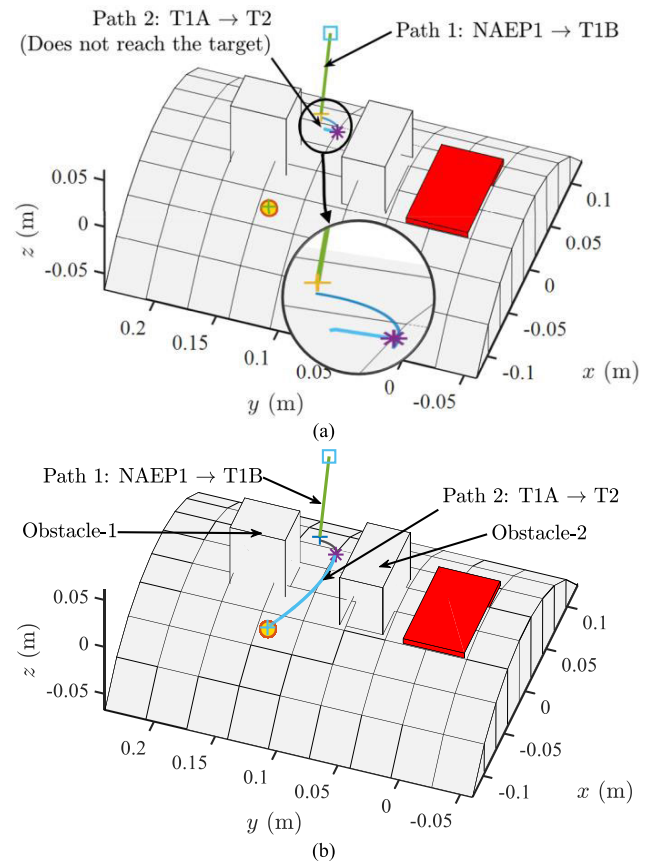

(a)

(b)

FIGURE 19. Op. 4 (a) Desired paths and points of two tasks on the workpiece using APF method. (b) Desired paths and points of three tasks on the workpiece using MAPF method.
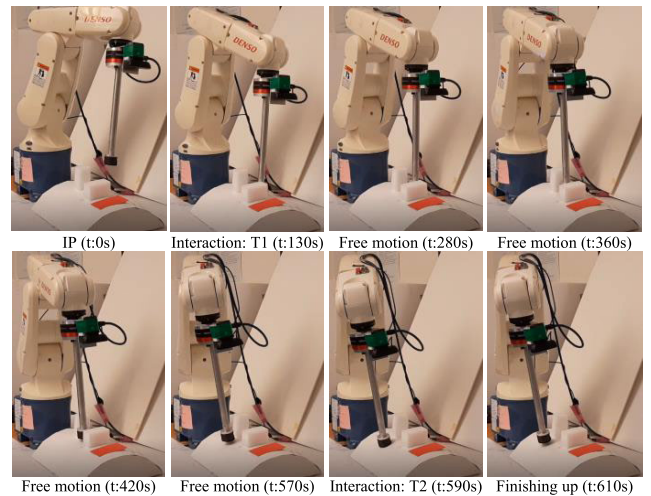

IP (t:0s)   Interaction: T1 (t:130s)   Free motion (t:280s)   Free motion (t:360s)

Free motion (t:420s)   Free motion (t:570s)   Interaction: T2 (t:590s)   Finishing up (t:610s)

FIGURE 20. The robot operating Op. 4.

The results of tracking the image feature and interaction force and joint velocities are demonstrated in FIGURE 24-FIGURE 26, respectively. In FIGURE 24, the FQSMC tracks the desired image feature signals with higher precision, lower chattering, oscillation, and faster convergence speed compared with SMC and even P/PI. SMC tracks
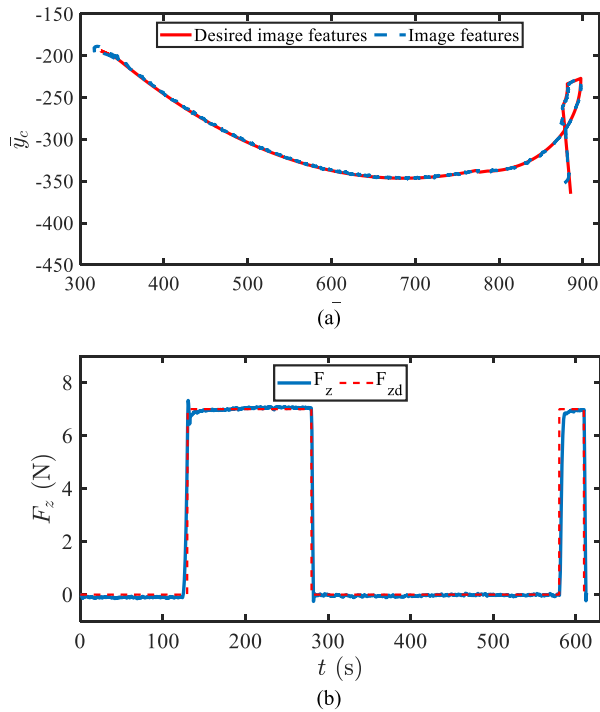
FIGURE 21. Path tracking in the image space and force control of all the tasks of OP. 4. (a) Tracking the paths and points in the image space of Op. 1. (b) Controlling the force of Op. 4.
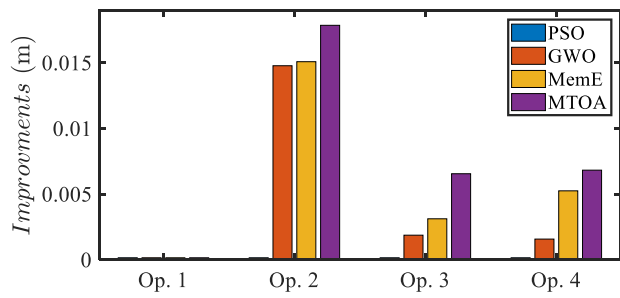

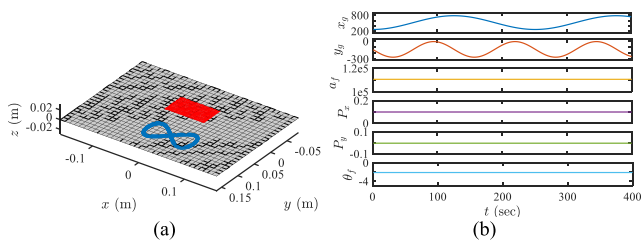**FIGURE 22.** Improvement percentage of the optimization methods.

FIGURE 23. Test 5 (a) Desired path on the workpiece. (b) Corresponding feature.

the signals with higher precision relative to P/PI. However, the chattering level of the P/PI is much lower. FIGURE 25 shows the superiority of the FQSMC to P/PI and SMC in terms of chattering level, tracking precision, and convergence speed. The chattering issue is highlighted in the controller output, i.e., joint velocities, presented in FIGURE 26.
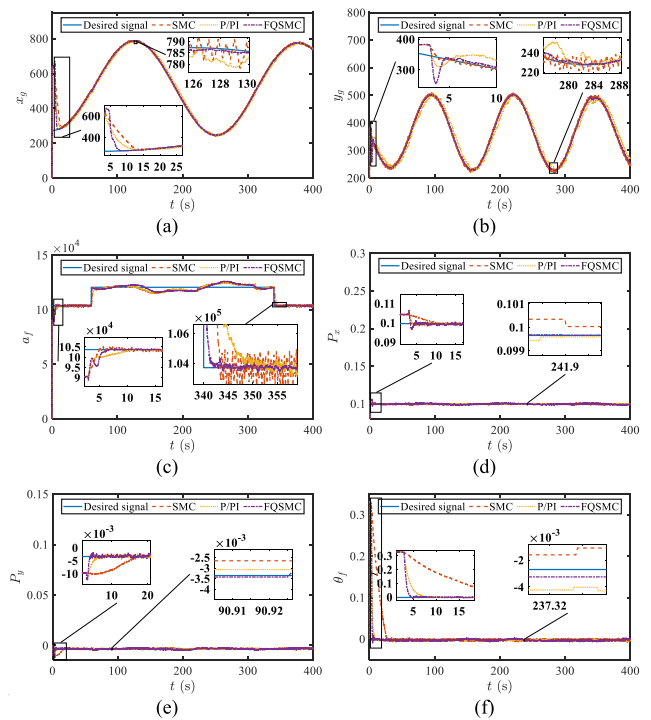

FIGURE 24. Tracking image features of the third test (a) $\bar{x}$. (b) $\bar{y}$. (c) a_f. (d) S_x. (e) S_y. f) θ_f.
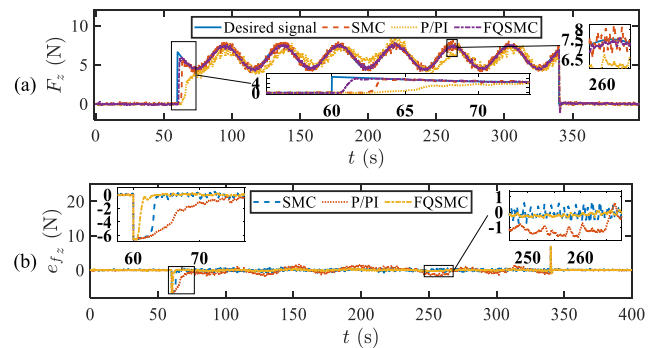

FIGURE 25. Force control of the third test.

SMC suffers from a high level of chattering, while the P/PI produces less chattering, and FQSMC's output is rather smooth. Note that, for SMC, the chattering is emanated from the switching function in the control law and the existing noise of the sensors' feedbacks. Whereas the chattering in the P/PI's output is only due to the noises. The reason is the level of chattering in P/PI is lower compared with that in SMC. FQSMC, on the other hand, has an intrinsic filter and does not employ any switching function in its control law. Consequently, it generates a smooth control command.

In addition to the plots, several numerical indicators such as integral absolute error (IAE), integral time absolute error (ITAE), standard deviation (STD), and root mean square error (RMSE) indicators are selected for quantitative comparison in terms of vision and force errors [20]. On the other
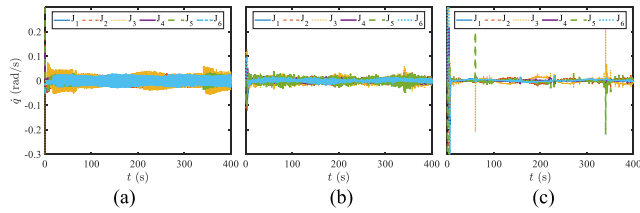
FIGURE 26. Robot joint velocities (test 3) (a) SMC. (b) P/PI. (c) FQSMC.

TABLE 3. The computed values of the indicators for the norms of system errors of the third test.

	Comp.	Indicator			
		IAE	ITAE	STD	RMSE
Vision	P	0.2069	39.0753	0.0003	0.0006
	SMC	0.1355	12.386	1.10e-4	1.15e-4
	FQSMC	0.0660	7.334	3.4e-5	3.8e-5
Force	PI	201.85	36239.4	0.7643	0.7898
	SMC	158.95	24956.4	0.8724	0.8979
	FQSMC	63.731	10379.4	0.5283	0.5335

TABLE 4. The computed values of the indicators for the controller output of the third test.

Indicator	Compensator		
	P/PI	SMC	FQSMC
STD	0.018499	0.029509	0.005577
ISCO	0.700458	1.436190	0.385108

hand, STD and integral square controller output (ISCO) indicators are evaluated for the joint velocities (controller output). These indicators are computed for the third test and tabulated in TABLE 3 and TABLE 4. Note that since the dimension of the vision and joint velocity results is higher than one (it is six), the weighted norms of the vision and joint velocity are used to compute those indicators.

Referring to TABLE 3, for the vision control, FQSMC has decreased the values of IAE, ITAE, STD, and RMSE by 51.29%, 40.79%, 69.09%, and 66.96% compared to SMC, respectively. Compared to P/PI, these values are over 68.10%, 81.23%, 88.67%, and 93.67%. For the force control, FQSMC has decreased the values of IAE, ITAE, STD, and RMSE by 59.91%, 58.41%, 39.44%, and 40.58% compared to SMC, respectively. Compared to P/PI, these values are over 68.43%, 71.36%, 30.88%, and 32.45%. The results show that the proposed hybrid controller results in improvement of the control performance in terms of chattering, precision, and convergence rate to a significant extent.

Furthermore, according to TABLE 4, the values of STD and ISCO for FSMC are 81.1% and 73.19% lower in comparison with SMC, and 69.85% and 45.02% lower than those of the P/PI. These results show that FQSMC outperforms both SMC and P/PI in terms of chattering level and control effort.

VI. CONCLUSION

In this study, a novel image-based task-sequence/path planning method (MAPF-CGTSP) along with a robust vision/force control method is presented for industrial robots

to perform multi-task operations while interacting with a workpiece. The proposed MAPF-CGTSP algorithm combines a novel modified artificial potential field and a constrained generalized traveling salesman problem to achieve an optimal sequence of performing the tasks while generating a feasible and safe path between tasks for a multi-task operation. A mix-integer MTOA is developed to solve the proposed MAPF-CGTSP problem to achieve the integer sequence of performing the tasks and the continuous parameters of the MAPF method. Different test scenarios are employed to evaluate the MAPF-CGTSP algorithm combined with the vision/force control method. The results obtained in the different environments demonstrate that the proposed method can perform the multi-task operations using vision/force control method in different environments which makes it a suitable algorithm to be employed in industrial applications dealing with complex and real scenarios. The experimental results demonstrate that the MTOA algorithm yields better solutions in all the test environments compared to the other optimization methods. Also, the path planning results of the MAPF method are improved compared to the traditional APF. Another advantage of the proposed method is developing the FQSMC for vision/force control of industrial robots exploiting an intrinsic low-pass filter which leads to filtering out the measurement noises associated with the camera and force sensor. Also, the proposed controller results in Quasi-motion and elimination of chattering compared to the other provided methods which make it reliable in real-world scenarios. The experimental results show the benefits of the proposed MAPF-CGTSP algorithm for task sequence/path planning combined with the vision/force control in multi-task operations. The performance of the proposed MAPF-CGTSP method has been assessed in the first test using the test environments composed of different configurations and several obstacles. Also, the performance of the proposed vision/force control approach is compared with that of the other control methods to show its effectiveness. The results show the effectiveness of the proposed MAPF-CGTSP method in terms of collision avoidance and provide a safe and feasible path compared to the other methods. Also, the superiority of the proposed vision/force method to other well-known methods is evaluated in terms of precision, convergence rate, robustness, control effort, and chattering.

In future work, it could be interesting to focus on the problem of the camera's field-of-view limitation, since this work assumes that the features are always in the field of view. Another future work is considering the use of the proposed MAPF-CGTSP method for multi-robot task sequence/path planning since this work only considers one robot. However, in real applications, it may be required to make cooperation between several robots.

REFERENCES

[1] C. Wong, C. Mineo, E. Yang, X.-T. Yan, and D. Gu, "A novel clustering-based algorithm for solving spatially constrained robotic task sequencing problems," *IEEE/ASME Trans. Mechatronics*, vol. 26, no. 5, pp. 2294–2305, Oct. 2021, doi: 10.1109/TMECH.2020.3037158.

[2] X. Wang, Y. Shi, D. Ding, and X. Gu, "Double global optimum genetic algorithm–particle swarm optimization-based welding robot path planning," *Eng. Optim.*, vol. 48, no. 2, pp. 299–316, Feb. 2016.

[3] Z. Han, J. Allspaw, G. LeMasurier, J. Parrillo, D. Giger, S. R. Ahmadzadeh, and H. A. Yanco, "Towards mobile multi-task manipulation in a confined and integrated environment with irregular objects," in *Proc. IEEE Int. Conf. Robot. Autom. (ICRA)*, May 2020, pp. 11025–11031.

[4] P. Kurtser and Y. Edan, "Planning the sequence of tasks for harvesting robots," *Robot. Autom. Syst.*, vol. 131, Sep. 2020, Art. no. 103591.

[5] S. Diyaley, A. Aditya, and S. Chakraborty, "Optimization of the multi-hole drilling path sequence for concentric circular patterns," *Opsearch*, vol. 57, no. 3, pp. 746–764, Sep. 2020.

[6] A. Kovács, "Integrated task sequencing and path planning for robotic remote laser welding," *Int. J. Prod. Res.*, vol. 54, no. 4, pp. 1210–1224, Feb. 2016.

[7] X. Xu, Y. Hu, J. M. Zhai, L. Z. Li, and P. S. Guo, "A novel non-collision trajectory planning algorithm based on velocity potential field for robotic manipulator," *Int. J. Adv. Robot. Syst.*, vol. 15, no. 4, pp. 1–13, Jul. 2018.

[8] S.-O. Park, M. C. Lee, and J. Kim, "Trajectory planning with collision avoidance for redundant robots using Jacobian and artificial potential field-based real-time inverse kinematics," *Int. J. Control, Autom. Syst.*, vol. 18, no. 8, pp. 2095–2107, Aug. 2020.

[9] T. Zhao, H. Li, and S. Dian, "Multi-robot path planning based on improved artificial potential field and fuzzy inference system1," *J. Intell. Fuzzy Syst.*, vol. 39, no. 5, pp. 7621–7637, Nov. 2020.

[10] I. Can, "Position/force control of robot manipulators," M.S. thesis, Dept. Mech. Eng., METU, Ankara, Turkey, 2003.

[11] E. Lutscher, E. C. Dean-Leon, and G. Cheng, "Hierarchical force and positioning task specification for indirect force controlled robots," *IEEE Trans. Robot.*, vol. 34, no. 1, pp. 280–286, Feb. 2018.

[12] H. Navvabi and A. H. D. Markazi, "Hybrid position/force control of stewart manipulator using extended adaptive fuzzy sliding mode controller (E-AFSMC)," *ISA Trans.*, vol. 88, pp. 280–295, May 2019.

[13] Y. Zhang, C. Hua, and J. Qian, "Adaptive robust visual servoing/force control for robot manipulator with dead-zone input," *IEEE Access*, vol. 7, pp. 129627–129636, 2019.

[14] X. Yu, W. He, Q. Li, Y. Li, and B. Li, "Human-robot co-carrying using visual and force sensing," *IEEE Trans. Ind. Electron.*, vol. 68, no. 9, pp. 8657–8666, Sep. 2021, doi: 10.1109/TIE.2020.3016271.

[15] H. Wang, H. Ni, J. Wang, and W. Chen, "Hybrid vision/force control of soft robot based on a deformation model," *IEEE Trans. Control Syst. Technol.*, vol. 29, no. 2, pp. 661–671, Mar. 2021.

[16] J. Baeten, H. Bruyninckx, and J. D. Schutter, "Tool/camera configurations for eye-in-hand hybrid vision/force control," in *Proc. IEEE Int. Conf. Robot. Autom.*, Washington, DC, USA, May 2002, pp. 1704–1709.

[17] Y. Chang, L. Li, Y. Wang, and K. You, "Toward fast convergence and calibration-free visual servoing control: A new image based uncalibrated finite time control scheme," *IEEE Access*, vol. 8, pp. 88333–88347, 2020.

[18] A. Ghasemi, P. Li, and W.-F. Xie, "Adaptive switch image-based visual servoing for industrial robots," *Int. J. Control Autom. Syst.*, vol. 18, no. 5, pp. 1324–1334, 2019.

[19] F. Chaumette and S. Hutchinson, "Visual servo control. I. Basic approaches," *IEEE Robot. Autom. Mag.*, vol. 13, no. 4, pp. 82–90, Dec. 2006.

[20] E. Zakeri, S. A. Moezi, and M. Eghtesad, "Optimal interval type-2 fuzzy fractional order super twisting algorithm: A second order sliding mode controller for fully-actuated and under-actuated nonlinear systems," *ISA Trans.*, vol. 85, pp. 13–32, Feb. 2019.

[21] C.-F. Huang, T.-L. Liao, C.-Y. Chen, and J.-J. Yan, "The design of quasi-sliding mode control for a permanent magnet synchronous motor with unmatched uncertainties," *Comput. Math. Appl.*, vol. 64, pp. 1036–1043, Sep. 2012.

[22] F. Schramm and G. Morel, "Ensuring visibility in calibration-free path planning for image-based visual servoing," *IEEE Trans. Robot.*, vol. 22, no. 4, pp. 848–854, Aug. 2006.

[23] M. Keshmiri and W.-F. Xie, "Image-based visual servoing using an optimized trajectory planning technique," *IEEE/ASME Trans. Mechatronics*, vol. 22, no. 1, pp. 359–370, Feb. 2017.

[24] B. Ahmadi, W.-F. Xie, and E. Zakeri, "Robust cascade Vision/Force control of industrial robots utilizing continuous integral sliding-mode control method," *IEEE/ASME Trans. Mechatronics*, vol. 27, no. 1, pp. 524–536, Feb. 2022, doi: 10.1109/TMECH.2021.3067619.

[25] A. Vakanski, F. Janabi-Sharifi, and I. Mantegh, "An image-based trajectory planning approach for robust robot programming by demonstration," *Robot. Auton. Syst.*, vol. 98, pp. 241–257, Dec. 2017.

[26] M. T. Hagan, H. B. Demuth, and M. Beale, *Neural Network Design*. New Delhi, India: PWS, 1996.

[27] L. Villani and J. De Schutter, "Force Control," in *Springer Handbook Robotics*, B. Siciliano O. Khatib, Eds. Berlin, Germany: Springer, 2008, pp. 161–185.

[28] M. G. Krishnan and S. Ashok, "Adaptive gain control law for visual servoing of 6DOF robot manipulator," in *Proc. Int. Conf. Control, Power, Commun. Comput. Technol. (ICCPCCT)*, Kannur, Mar. 2018, pp. 57–64.

[29] S. M. Kay, *Fundamentals of Statistical Signal Processing: Estimation Theory*. Upper Saddle River, NJ, USA: Prentice-Hall, 1993.

[30] S. S. Ge and Y. J. Cui, "Dynamic motion planning for mobile robots using potential field method," *Auto. Robots*, vol. 13, no. 3, pp. 207–222, 2002.

[31] J. S. Smith, B. Wu, and B. M. Wilamowski, "Neural network training with Levenberg–Marquardt and adaptable weight compression," *IEEE Trans. Neural Netw. Learn. Syst.*, vol. 30, no. 2, pp. 580–587, Feb. 2019.

[32] I. Mohsin, K. He, Z. Li, and R. Du, "Path planning under force control in robotic polishing of the complex curved surfaces," *Appl. Sci.*, vol. 9, no. 24, p. 5489, Dec. 2019.

[33] F. Tian, C. Lv, Z. Li, and G. Liu, "Modeling and control of robotic automatic polishing for curved surfaces," *CIRP J. Manuf. Sci. Technol.*, vol. 14, pp. 55–64, Aug. 2016.

[34] F. Tian, Z. Li, C. Lv, and G. Liu, "Polishing pressure investigations of robot automatic polishing on curved surfaces," *Int. J. Adv. Manuf. Technol.*, vol. 87, nos. 1–4, pp. 639–646, Oct. 2016.

[35] S. Hutchinson, G. D. Hager, and P. I. Corke, "A tutorial on visual servo control," *IEEE Trans. Robot. Autom.*, vol. 12, no. 5, pp. 651–670, Oct. 1996.

[36] M. A. Fischler and R. Bolles, "Random sample consensus: A paradigm for model fitting with applications to image analysis and automated cartography," *Commun. ACM*, vol. 24, no. 6, pp. 381–395, 1981.

[37] N. X. Quynh, W. Y. Nan, and V. T. Yen, "Design of a robust adaptive sliding mode control using recurrent fuzzy wavelet functional link neural networks for industrial robot manipulator with dead zone," *Intell. Service Robot.*, vol. 13, no. 2, pp. 219–233, Apr. 2020.

[38] K. Shojaei, A. Kazemy, and A. Chatraei, "An observer-based neural adaptive PID 2 controller for robot manipulators including motor dynamics with a prescribed performance," *IEEE/ASME Trans. Mechatronics*, vol. 26, no. 3, pp. 1689–1699, Jun. 2021.

[39] A. San-Miguel, V. Puig, and G. Alenyá, "Disturbance observer-based LPV feedback control of a N-DoF robotic manipulator including compliance through gain shifting," *Control Eng. Pract.*, vol. 115, Oct. 2021, Art. no. 104887.

[40] K. Shojaei, "An adaptive output feedback proportional-integral-derivative controller for n-Link type (m,s) electrically driven mobile manipulators," *J. Dyn. Syst., Meas., Control*, vol. 141, no. 9, Sep. 2019, Art. no. 091001.

[41] J. Feddema and O. Mitchcll, "Vision-guided servoing with feature-based trajectory generation," *IEEE Trans. Robot. Automat.*, vol. 5, no. 5, pp. 691–700, Oct. 1989.

[42] J. T. Feddema, C. S. G. Lee, and O. R. Mitchell, "Weighted selection of image features for resolved rate visual feedback control," *IEEE Trans. Robot. Autom.*, vol. 7, pp. 31–47, Feb. 1991.

[43] L. Weiss, A. Sanderson, and C. Neuman, "Dynamic sensor-based control of robots with visual feedback," *IEEE J. Robot. Autom.*, vol. JRA-3, no. 5, pp. 404–417, Oct. 1987.

[44] B. H. Yoshimi and P. K. Allen, "Active, uncalibrated visual servoing," in *Proc. IEEE Int. Conf. Robot. Autom.*, San Diego, CA, USA, May 1994, pp. 156–161.

[45] U. Orozco-Rosas, K. Picos, and O. Montiel, "Hybrid path planning algorithm based on membrane pseudo-bacterial potential field for autonomous mobile robots," *IEEE Access*, vol. 7, pp. 156787–156803, 2019.

[46] U. Orozco-Rosas, O. Montiel, and R. Sepúlveda, "Mobile robot path planning using membrane evolutionary artificial potential field," *Appl. Soft Comput. J.*, vol. 77, pp. 236–251, Apr. 2019.

[47] A. A. Ahmed, T. Y. Abdalla, and A. A. Abed, "Path planning of mobile robot by using modified optimized potential field method," *Int. J. Comput. Appl.*, vol. 113, no. 4, pp. 6–10, Mar. 2015.

[48] A. Azzabi and K. Nouri, "An advanced potential field method proposed for mobile robot path planning," *Trans. Inst. Meas. Control*, vol. 41, no. 11, pp. 3132–3144, Jul. 2019.

[49] H. Khosravi, E. Zakeri, W.-F. Xie, and B. Ahmadi, "Adaptive multi-tracker optimization algorithm for global optimization problems: Emphasis on applications in chemical engineering," *Eng. Comput.*, vol. 2020, pp. 1–28, Jul. 2020.

[50] S. Katoch, S. S. Chauhan, and V. Kumar, "A review on genetic algorithm: Past, present, and future," *Multimedia Tools Appl.*, vol. 80, pp. 8091–8126, Oct. 2020.

[51] F. Wang, H. Zhang, and A. Zhou, "A particle swarm optimization algorithm for mixed-variable optimization problems," *Swarm Evol. Comput.*, vol. 60, Feb. 2021, Art. no. 100808.

[52] P. Hao and B. Sobhani, "Application of the improved chaotic grey wolf optimization algorithm as a novel and efficient method for parameter estimation of solid oxide fuel cells model," *Int. J. Hydrogen Energy*, vol. 46, no. 73, pp. 36454–36465, Oct. 2021.

[53] E. Zakeri, S. A. Moezi, Y. Bazargan-Lari, and A. Zare, "Multi-tracker optimization algorithm: A general algorithm for solving engineering optimization problems," *Iranian J. Sci. Technol., Trans. Mech. Eng.*, vol. 41, no. 4, pp. 315–341, Dec. 2017, doi: 10.1007/s40997-016-0066-9.

BAHAR AHMADI received the M.Sc. degree in industrial control systems from Tabriz University, in 2014. She is currently pursuing the Ph.D. degree in vision/force control of industrial robots with Concordia University, Montreal, QC, Canada. She was an Active Member of the Dynamic and Robotic Research Group, Tabriz University. She has been involved in several projects of the group. Her research interests include robotics and control, machine vision, machine learning, and nonlinear systems.

EHSAN ZAKERI received the M.Sc. degree in mechatronics from Sistan and Baluchistan University, in 2015. He is currently pursuing the Ph.D. degree in intelligent hybrid vision/force control of medical/industrial robots with Concordia University, Montreal, QC, Canada. His research interests include robotics and mechatronics, visual servoing, automatic control, optimization, soft computing, and artifice intelligence.
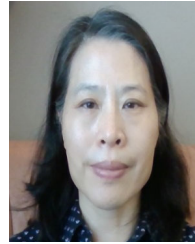
WEN-FANG XIE (Senior Member, IEEE) received the master's degree in flight navigation and control from Beihang University, in 1991, and the Ph.D. degree from the Department of Electrical Engineering, The Hong Kong Polytechnic University, in 1999. She is currently a Professor with the Department of Mechanical, Industrial and Aerospace Engineering, Concordia University, Montreal, Canada. She joined Concordia University as an Assistant Professor, in 2003, and was promoted to an Associate Professor and a Professor, in 2008 and 2014, respectively. Her research interests include nonlinear control and identification in mechatronics, visual servoing, model predictive control, neural networks, advanced process control, and system identification.

• • •